# THE EFFECT OF ION-ORBIT-LOSS ON THE DISTRIBUTION OF ION, ENERGY AND MOMENTUM FROM THE EDGE PLASMA INTO THE SCRAPE-OFF LAYER IN TOKAMAKS

A Thesis
Presented to
The Academic Faculty

by

Matthew Thomas Schumann

In Partial Fulfillment
of the Requirements for the Degree
Masters of Science in the
Nuclear and Radiological Engineering Program
School of Mechanical Engineering

Georgia Institute of Technology

May 2015

# THE EFFECT OF ION-ORBIT-LOSS ON THE DISTRIBUTION OF ION, ENERGY AND MOMENTUM FROM THE EDGE PLASMA INTO THE SCRAPE-OFF LAYER IN TOKAMAKS

Approved by:

Dr. Weston, Stacey – Advisor
Nuclear and Radiological Engineering Program
School of Mechanical Engineering
*Georgia Institute of Technology*

Dr. Bojan, Petrovic
Nuclear and Radiological Engineering Program
School of Mechanical Engineering
*Georgia Institute of Technology*

Dr. Dingkang, Zhang
Nuclear and Radiological Engineering Program
School of Mechanical Engineering
*Georgia Institute of Technology*

Date Approved: January 28, 2015

# ACKNOWLEDGEMENTS

I wish to thank Dr. Stacey for guiding and directing my research, Theresa Wilks for suggestions on different ways to approach ion-orbit-loss fractions, and Tim Collart for helping me work through the complexities of multidimensional matrix manipulation.

# TABLE OF CONTENTS

CHAPTER

# LIST OF TABLES

Page

# LIST OF FIGURES

# LIST OF SYMBOLS

| | |
|---|---|
| $\theta_0$ | Poloidal launch position on an inner flux surface |
| $\rho_0$ | Internal flux surface position |
| $\zeta_0$ | Cosine of initial guiding center velocity relative to the toroidal magnetic field |
| $\theta_S$ | Poloidal exit position on the separatrix |
| $V_{\|\|}$ | Parallel velocity component |
| $V_\perp$ | Perpendicular velocity component |
| $e$ | Electric charge |
| $\phi$ | Electrostatic potential |
| $\mathrm{B}_\varphi$ | Toroidal magnetic field |
| $R$ | Major radius |
| $f_\varphi$ | Magnetic field ratio |
| $I$ | Plasma Current |
| $a$ | Horizontal minor radius |
| $\kappa$ | Elongation |
| $T_{ion}$ | Ion temperature |
| $E_{min}$ | Minimum energy |
| $\varepsilon_{min}$ | Minimum reduced energy |
| $f$ | Directional sampling factor |
| $\Gamma$ | Complete Gamma function |
| $\gamma$ | Incomplete Gamma function |
| $F$ | Ion loss fraction |
| $M$ | Momentum loss fraction |
| $E$ | Energy loss fraction |

# LIST OF ABBREVIATIONS

| | |
|---|---|
| IOL | Ion-Orbit-Loss |
| SOL | Scrape-Off Layer |
| H-Mode | High-Mode |
| PDF | Probability Distribution Function |

# SUMMARY

Some of the outflowing ions in the tokamak plasma edge have sufficient energy to access orbits which allow them to free-stream out of the confined plasma region and be lost to the wall or divertor. The effects of this ion-orbit-loss (IOL) on the poloidal distribution of ion, energy and momentum fluxes from the plasma edge into the surrounding tokamak scrape-off layer (SOL) are analyzed for a representative DIII-D H-mode discharge. IOL yields large fluxes of particle, energy and momentum, distributed poloidally over the SOL, but predominantly into the outboard SOL. The net fluxes into the SOL resulting from IOL and transport within the plasma have a significantly different poloidal distribution than the fluxes resulting from transport processes with the plasma alone. An intrinsic co-current rotation in the edge of the plasma is produced by the preferential IOL loss of counter-current ions.

# CHAPTER 1

# INTRODUCTION

Ions which execute orbits that cross the last closed flux surface (or separatrix) and leave the plasma are an important loss mechanism in the edge plasma region of tokamaks. Such loss affects the radial electric field, energy and particle confinement, poloidal and toroidal rotation, the interpretation of conductive/diffusive transport coefficients, as well as other variables for confined plasmas [eg. References 1–9]. This ion-orbit-loss (IOL) will also affect the poloidal distribution of particle, energy and momentum sources from the edge plasma into the scrape-off layer (SOL) and thus the physical properties (temperature and density distributions, etc) in the SOL and into the divertor. The poloidal distribution of these fluxes out of the plasma is important for heat removal design of future tokamaks. In this thesis we investigate the effects of IOL on the poloidal distribution of ion, energy and parallel momentum into the SOL from the edge region of the plasma, for a representative DIII-D [13] H-mode plasma. We will focus on the method for calculating these IOL effects in fully differential form, which is a major new development of this thesis.

The thesis will be organized as follows. The basic ion orbit loss calculation of the minimum energy that an ion located on an internal flux surface, with a given directional cosine relative to the toroidal magnetic field, must have in order to execute a drift orbit that crosses the separatrix is described in chapter 2. The computational methodology is that introduced by Miyamoto [6] and extended for numerical computation by Stacey [10-14]. We will also introduce the four variables with respect to which we will characterize the ion-orbit-loss: directional cosine with respect to toroidal field $\zeta_0$, poloidal exit location on the separatrix $\theta_S$, poloidal launch location from an internal flux surface $\theta_0$ and internal 'radial' flux surface position $\rho_0$.

We first describe a sample calculation for a set of ions to illustrate the use of this basic IOL calculation and its impacts on the overall energy distribution in chapter 3. Once the basic ion orbit loss calculation has been completed for an example set of ions, at a flux surface near the edge of the plasma, we calculate a differential (with respect to direction-cosine, poloidal position and radius) loss zone within the thermal plasma ion distribution at each flux surface, poloidal position and directional cosine.

For the purposes of the calculation the ions are assumed to be lost from the main confined plasma body if at any location they cross the separatrix, due to either interaction with ions and neutrals in the SOL, an impact with the 1st wall, or being swept into the divertor. The ions in the loss zone for our example set are used to construct ion, particle and parallel momentum loss fractions in chapter 4. The sample calculation also demonstrates the allocation of the loss fractions over the poloidal loss locations, which is a major new development of this thesis, necessary for the calculation of the full differential loss fraction.

The effects of IOL on the poloidal distribution of ion and energy sources from the edge plasma into the SOL are discussed in chapter 5. The parallel momentum source into the SOL, as well as the intrinsic rotation in the edge of the main plasma resulting from the preferential IOL of counter-current ions, as shown by deGrassie et al. [15,16] , Stacey et al. [17,18] and Pan et al. [19,20], are calculated with the new model and discussed in chapter 6.

# CHAPTER 2

# BASIC ION ORBIT CALCULATION

The basic ion orbit calculation [10,13] is set up to determine the minimum required energy for an ion located at a particular poloidal position ($\theta_0$) on an internal flux surface ($\psi_0$) with a direction cosine ($\zeta_0$) ($\zeta_0 < 0$ co-current and $\zeta_0 > 0$ counter-current) in order to be able to execute an orbit which will cross the separatrix at a given poloidal location ($\theta_S$), see Figures 1 & 2. For an outward flowing plasma and a decreasing ion temperature, this minimum escape energy decreases with radius and the lost ions are replenished by outward flowing ions from an inward surface with a higher escape energy.

We define the directional cosine, relative to the toroidal magnetic $B_\varphi$, as $\zeta_0 > 0$ for the counter-current direction.

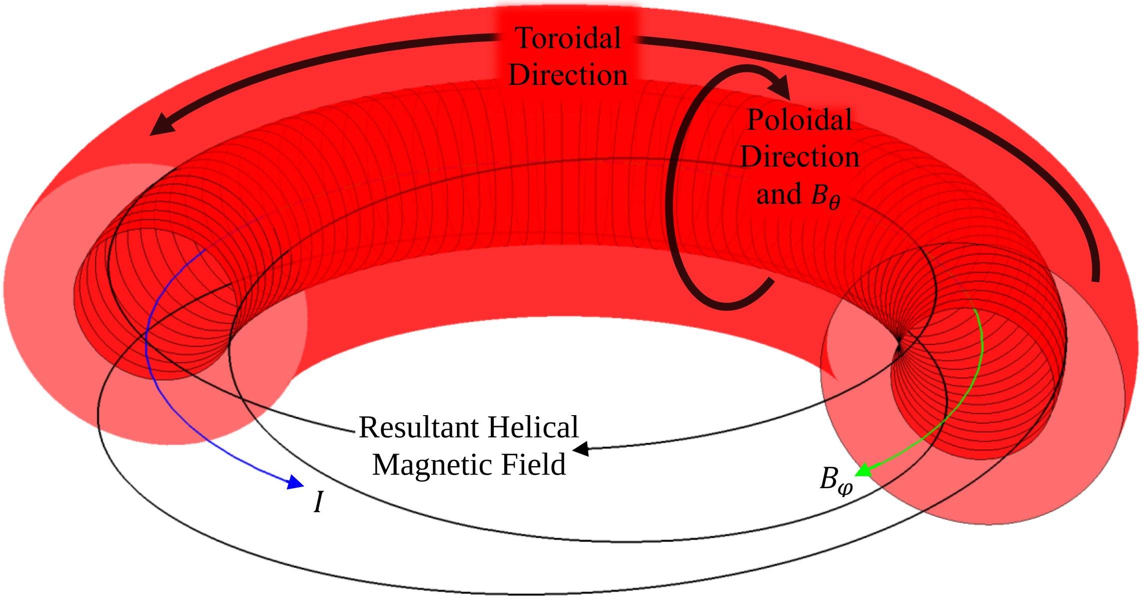

Figure 1. Poloidal and toroidal coordinates with toroidal magnetic field ($B_\varphi$), current ($I$) and the resultant magnetic field with poloidal field ($B_\theta$) directions in the tokamak plasma.

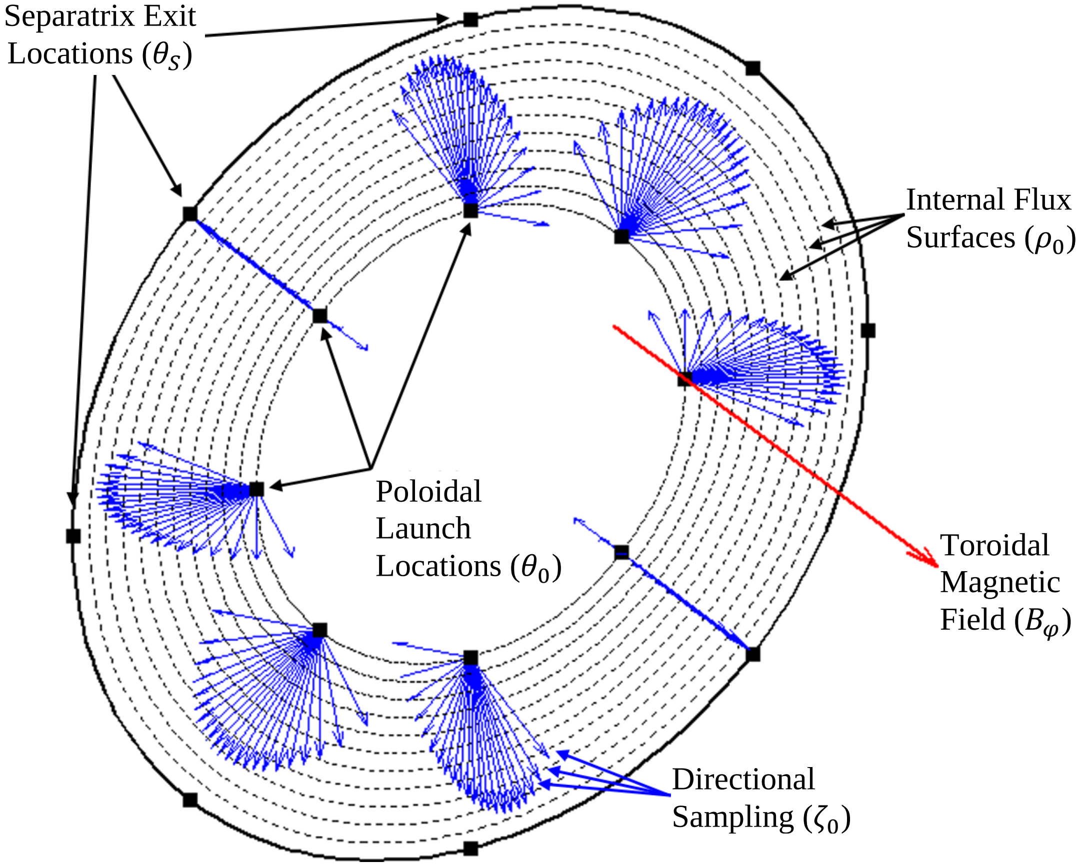

Figure 2. From the perspective of a poloidal cross section of the plasma at a fixed toroidal angle, $\varphi$, the poloidal launch and exit locations along with directions used for calculating minimum required energies for IOL to occur are shown.

Starting similarly as Miyamoto [6] and others we can use the conservation of energy, Equation (1), and magnetic moment, Equation (2) for an ion at a location $(\psi_0, \theta_0)$ with a parallel velocity component of $V_{||0}$

$$\frac{1}{2}m\left({V_{||}}^2 + {V_\perp}^2\right) + e\phi = const = \frac{1}{2}m\left(V_{||0}^2 + V_{\perp 0}^2\right) + e\phi_0 = \frac{1}{2}m{V_0}^2 + e\phi_0 \tag{1}$$

$$\frac{mV_\perp^2}{2B} = const = \frac{mV_{\perp 0}^2}{2B_0} \tag{2}$$

to solve for the parallel velocity $V_{||}$ given by

$$V_{||} = \pm V_0\left[1 - \left|\frac{B}{B_0}\right|\left(1 - \zeta_0^2\right) + \frac{2e}{mV_0^2}\left(\phi_0 - \phi\right)\right]^{1/2} \tag{3}$$

Making use of Equation (3) with the conservation of canonical toroidal angular momentum equation in the absence of scattering

$$RmV_{||}f_{\varphi} + e\phi = const = R_0 m V_{||} f_{\varphi 0} + e\psi_0 \tag{4}$$

and squaring leads to a quadratic equation for the initial ion speed (at $\psi_0$, $\theta_0$), $V_0 = \sqrt{V_{||0}^2 + V_{\perp 0}^2}$, required for the ion to execute an orbit which passes through a location $\theta_S$ on the separatrix, $\psi_s$.

$$V_0^2\left[\left(\left|\frac{R_0}{R}\right|\frac{f_{\varphi 0}}{f_{\varphi}}\zeta_0\right)^2 - 1 + (1-\zeta_0^2)\left|\frac{B}{B_0}\right|\right]$$

$$+V_0\left[\frac{2e(\psi_0-\psi)}{Rmf_{\varphi}}\left(\left|\frac{R_0}{R}\right|\frac{f_{\varphi 0}}{f_{\varphi}}\zeta_0\right)\right]$$

$$+\left[\left(\frac{e(\psi_0-\psi)}{Rmf_{\varphi}}\right)^2 - \frac{e(\phi_0-\phi)}{m}\right] = 0 \tag{5a}$$

Now for an ion with an initial poloidal location $\theta_0$ on an internal flux surface $\psi$ with a directional cosine relative to the toroidal magnetic field $B_{\varphi}$ given by $\zeta_0$, we can investigate whether this ion is capable of reaching an exit location $\theta_S$, on the separatrix $\psi_S$, by determining the minimum required speed for which Equation (5a) has a physically reasonable solution. For computational simplicity we now assume that $RB_{\varphi}$ is constant within the plasma. Thus a simplified equation may be written

$$V_0^2\left[\left(\left|\frac{B}{B_0}\right|\frac{f_{\varphi 0}}{f_{\varphi}}\zeta_0\right)^2 - 1 + (1-\zeta_0^2)\left|\frac{B}{B_0}\right|\right]$$

$$+V_0\left[\frac{2e(\psi_0-\psi)}{Rmf_{\varphi}}\left(\left|\frac{B}{B_0}\right|\frac{f_{\varphi 0}}{f_{\varphi}}\zeta_0\right)\right]$$

$$+\left[\left(\frac{e(\psi_0-\psi)}{Rmf_\varphi}\right)^2-\frac{e(\phi_0-\phi)}{m}\right]=0. \tag{5b}$$

Using the circular toroidal approximate representation of the magnetic flux surface geometry described by

$$\left[R(r,\theta)=\bar{R}h(r,\theta), B_{\theta,\varphi}(r,\theta)=\frac{\bar{B}_{\theta,\varphi}}{h(r,\theta)}, h(r,\theta)=(1+(r/\bar{R})\cos(\theta))\right], \tag{6}$$

making a uniform current density approximation in Ampere’s law, using $B_\theta=\nabla\times A_\varphi$ we can write the flux surface corresponding to a given effective circular normalized radius, $\psi$, as

$$\psi(\rho)=RA_\varphi=\frac{1}{2}\left(\frac{\mu_0 I}{2\pi a^2}\right)\bar{R}\bar{a}^2\rho^2. \tag{7}$$

These approximations are only valid when the inverse aspect ratio is much smaller than unity.

We solve Equation (5b) for the parameters of the DIII-D [21] H-mode plasma discharge shot #123302: (major plasma radius: $\bar{R}$ = 1.75 m, minor plasma radius: $\bar{a}$ = 0.885 m, elongation factor: $\kappa$ = 1.836, toroidal plasma current: $I$ = 1.50 MA, toroidal magnetic field: $B_\varphi$ = -1.98 T, safety factor: $q_{95}$ = 3.86, neutral beam power: $P_{nb}$ = 8.66 MW, carbon to deuterium number density fraction: $n_C/n_D$ = 0.03) The curvature and grad- $B$ drifts are vertically downward in this plasma towards a lower diverter.

In this plasma, the potential difference between some internal flux surface and the outermost last closed flux surface was obtained by solving for the local radial electric field via a radial carbon momentum balance using other measured carbon density, velocities and temperature. Then by integrating the radial electric field, we obtain the electrostatic potential. Some experimental data used in this calculation are shown in Figure 3.

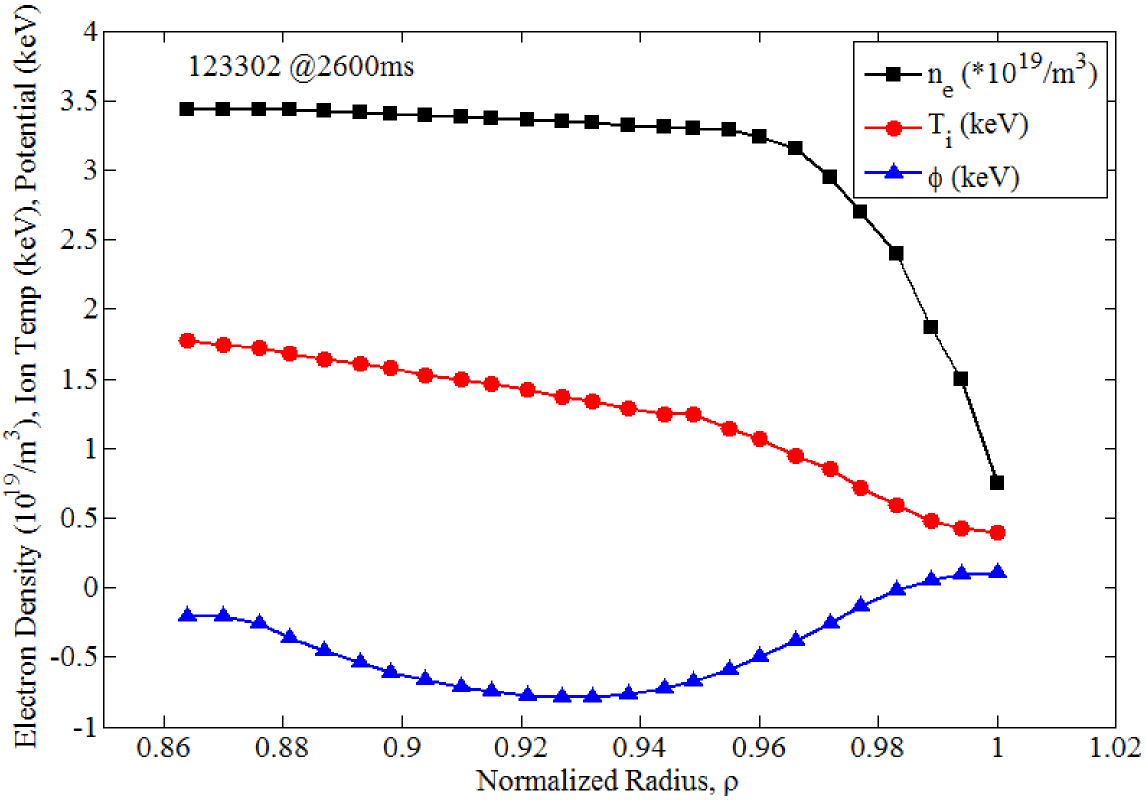

Figure 3. Electron density, ion temperature and electrostatic potential in the edge of DIII-D H-mode shot 123302.

# CHAPTER 3

# ION-ORBIT-LOSS MINIMUM ENERGY REQUIREMENTS

## Minimum Energy

The minimum reduced ion energy physically required for a particle with a directional cosine $\zeta_0$, at poloidal location $\theta_0$ on the internal flux surface $\rho_0 \equiv \bar{r}/\bar{a}$ to escape across the separatrix, $\rho_S = 1.0$, at poloidal location $\theta_S$ is given by

$$\varepsilon_{min}(\zeta_0, \theta_S, \theta_0, \rho_0) = \frac{E_{min}(\zeta_0,\theta_S,\theta_0,\rho_0)}{kT_{ion}(\rho_0)} = \frac{1/2 * m * V_{0\,min}^2(\zeta_0,\theta_S,\theta_0,\rho_0)}{kT_{ion}(\rho_0)}, \qquad (8)$$

where $V_{0\,min}$ is the minimum $V_0$ for which Equation (5b) has a physically reasonable solution and $E_{min} = 1/2 m V_{0min}^2$.

The minimum reduced energies so obtained describe the minimum required reduced energies for an ion launched from an internal flux surface $\rho_k \equiv \rho_0 < 1.0$, at a poloidal launch location $\theta_0$ ($0 \leq \theta_0 \leq 2\pi$) with directional cosine $\zeta_0$ to cross the separatrix ($\rho_S$ = 1.0) at a poloidal exit location $\theta_S$ ($0 \leq \theta_S \leq 2\pi$). See Figure 4 for an illustration of these locations. Eight different poloidal launch and exit locations are chosen (Figure 4) for the purpose of numerically evaluating the loss from all points on an inner surface through all points on the separatrix. The twenty two directional cosine $\zeta_0$ values (-1 $\leq \zeta_0 \leq$ 1), shown as the blue arrows in Figure 4 and Figure 2, were chosen to numerically divide the directional cosine into equally sized solid angle bins defined by their center values as discussed in Appendix A. The addition of more points to the numerical model for representing the lauch and exit locations or direction cosines did not significantly impact the resulting distributions. These directional bins define the differential angle. In the absence of scattering, which we assume, ions do not exchange among bins as they flow outward.

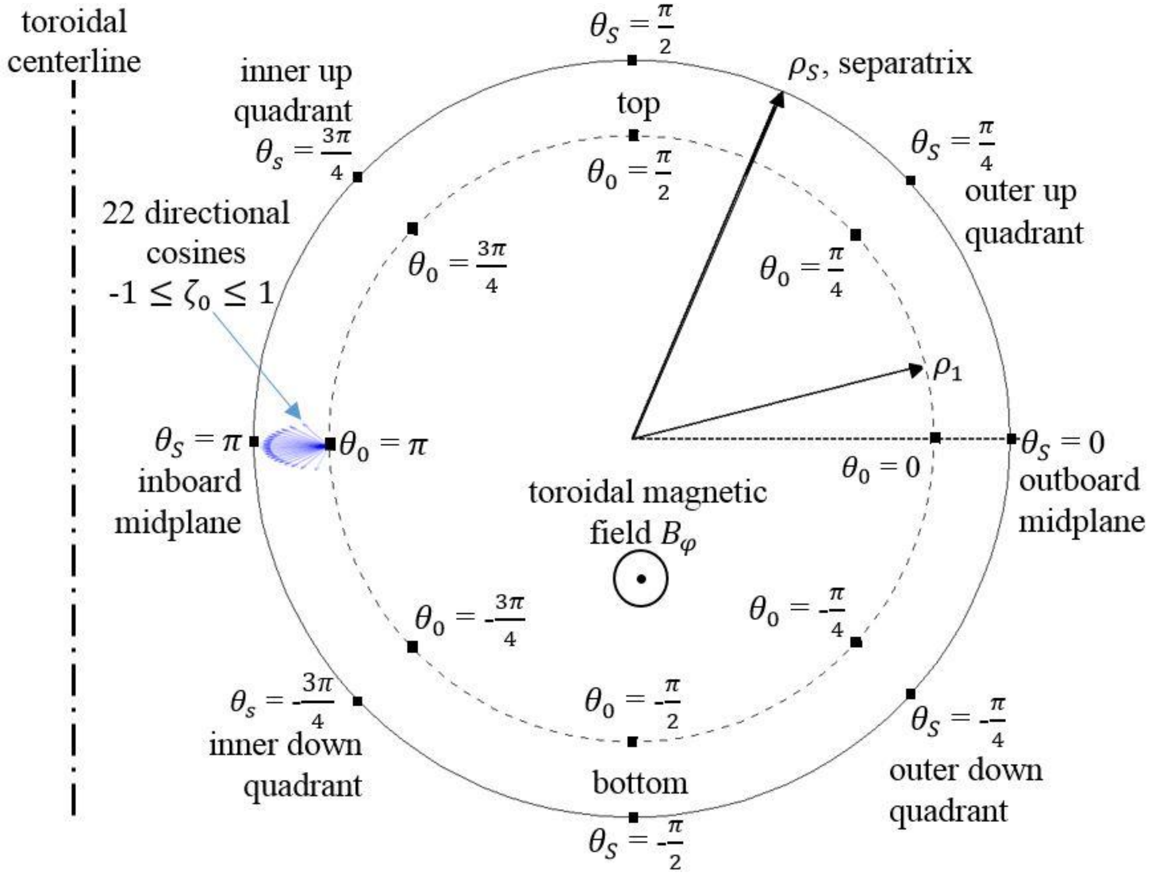

Figure 4. Location illustration for poloidal locations ($\theta_0$ internal) on the first flux surface ($\rho_1$), poloidal locations on the separatrix (and $\theta_S$ external), and a sample of the directional cosines ($\zeta_0$) with respect to $B_\varphi$.

The minimum energies calculated from Equation (8) are plotted in Figures 5-9 for the first flux surface, ($\rho_0$ = $\rho_1$ = 0.864, for all launch angle locations. Only the strongly counter-current ions ($\zeta_0 \gg 0$) were lost from most launch locations ($\theta_0$), and these were lost at the lowest $E_{min}$ through the outboard midplane escape location ($\theta_S = 0$). The co-current ($\zeta_0 < 0$) ions were lost significantly only from the inboard midplane launch location through the outboard midplane escape location (Figure 9). Also, shown for Figures 5-9 is, the surface minimum loss energies for all escape locations. Five similar results were calculated for other radial flux surface locations.

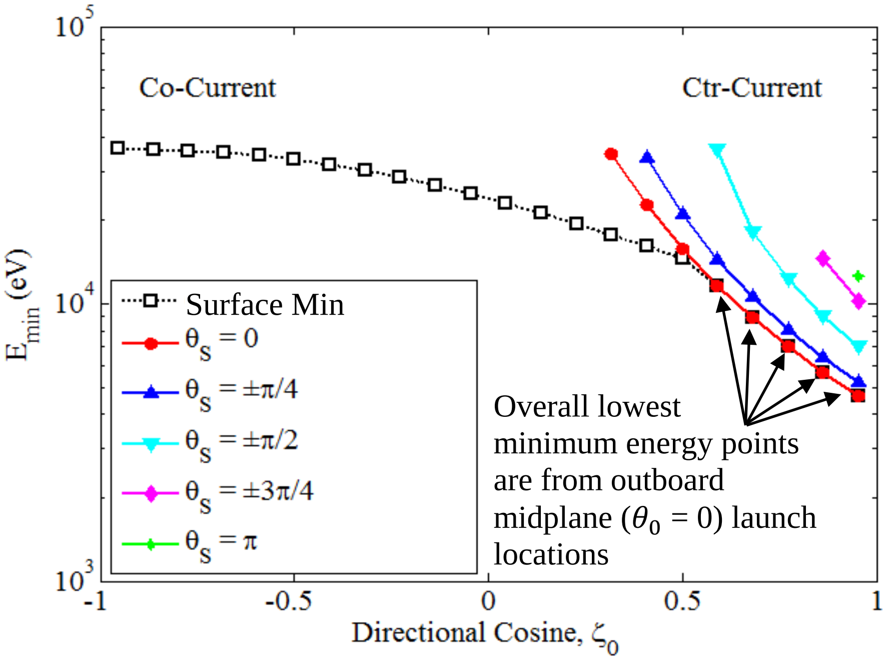

Figure 5. Minimum energy required for ion orbits from the first flux surface ($\rho_1$ = 0.864) at the outboard midplane launch location ($\theta_0$ = 0) to reach exit locations ($\theta_S$) on the separatrix ($\rho_S$ = 1.0). Also shown is the minimum lost energy for any launch location on the flux surface (dotted line with open squares).

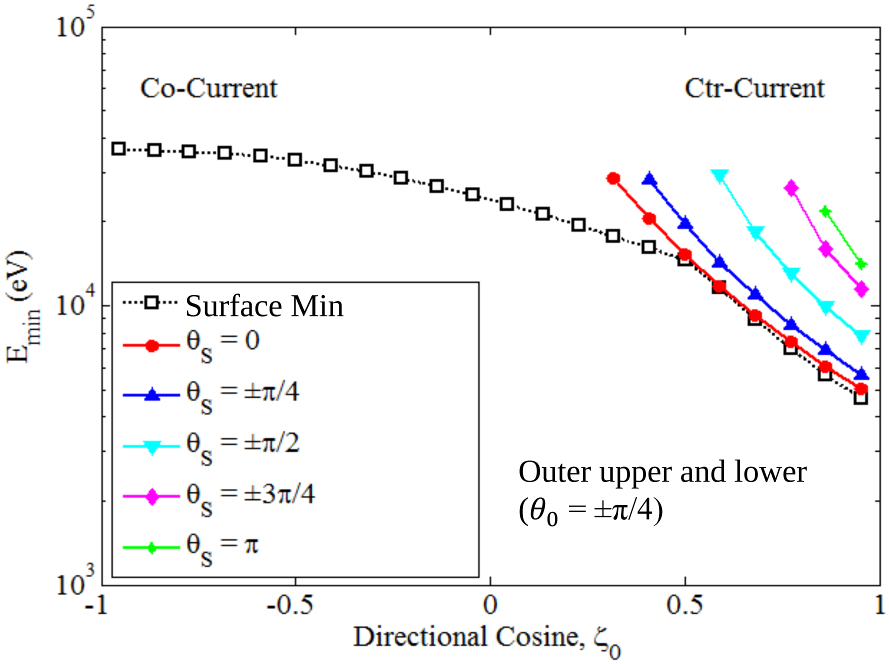

Figure 6. Minimum energy required for ion orbits from the first flux surface ($\rho_1 = 0.864$) at the outer upper and lower launch location ($\theta_0 = \pm\pi/4$) to reach exit locations ($\theta_S$) on the separatrix ($\rho_S = 1.0$). Also shown is the minimum lost energy for any launch location on the flux surface (dotted line with open squares).

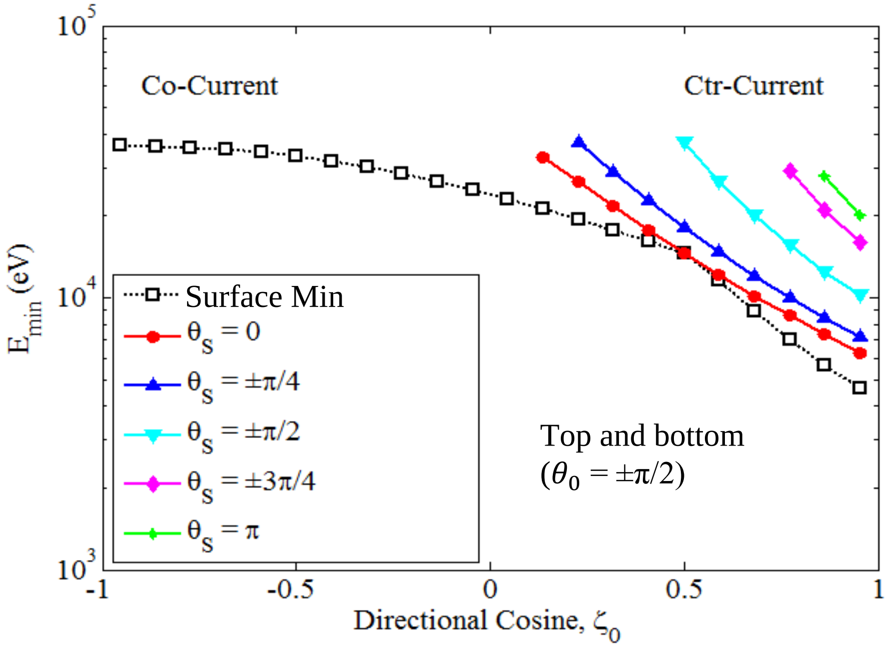

Figure 7. Minimum energy required for ion orbits from the first flux surface ($\rho_1 = 0.864$) at the top or bottom launch location ($\theta_0 = \pm\pi/2$) to reach exit locations ($\theta_S$) on the separatrix ($\rho_S = 1.0$). Also shown is the minimum lost energy for any launch location on the flux surface (dotted line with open squares).

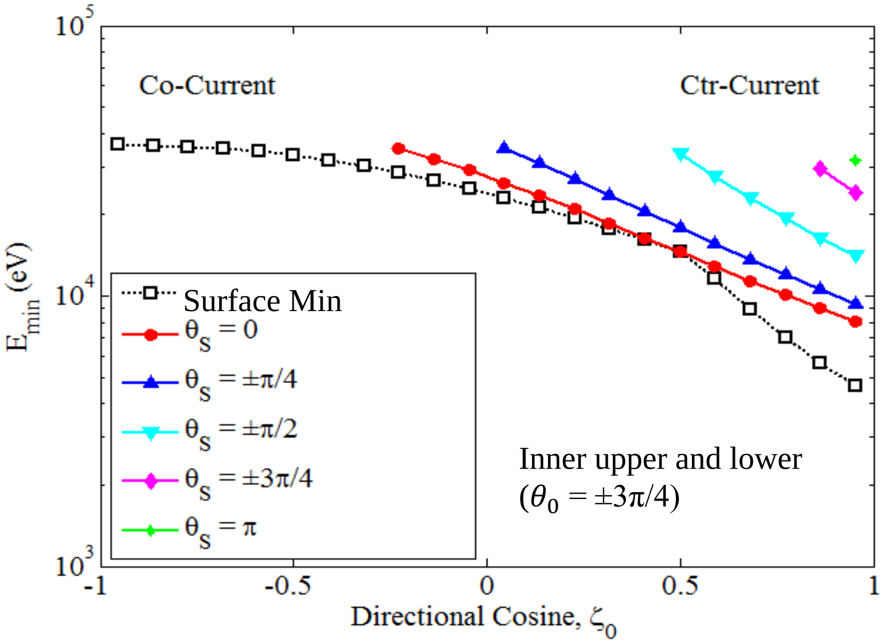

Figure 8. Minimum energy required for ion orbits from the first flux surface ($\rho_1 = 0.864$) at the inner upper and lower launch location ($\theta_0 = \pm3\pi/4$) to reach exit locations ($\theta_S$) on the separatrix ($\rho_S = 1.0$). Also shown is the minimum lost energy for any launch location on the flux surface (dotted line with open squares).

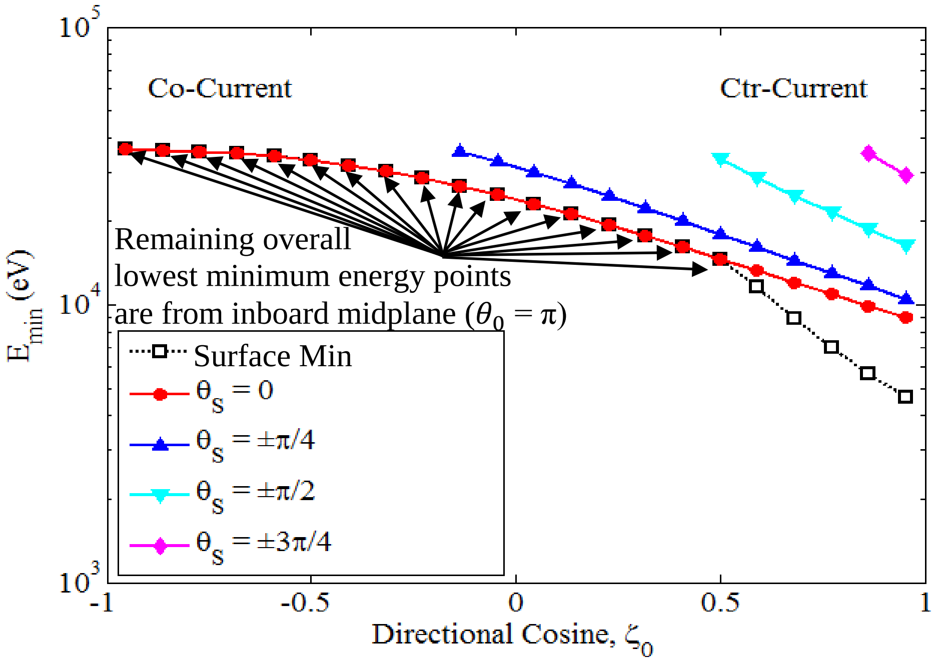

Figure 9. Minimum energy required for ion orbits from the first flux surface ($\rho_1 = 0.864$) at the inboard midplane launch location ($\theta_0 = \pi$) to reach exit locations ($\theta_S$) on the separatrix ($\rho_S = 1.0$). Also shown is the minimum lost energy for any launch location on the flux surface (dotted line with open squares).

The flux surface minimum energies (the dotted lines in Figures 5-9) for a few internal flux surfaces (at radial locations given by: $\rho_1$ = 0.864, $\rho_5$ = 0.887, $\rho_{10}$ = 0.915, $\rho_{15}$ = 0.944, $\rho_{20}$ = 0.972 and $\rho_{24}$ = 0.994) are plotted in Figure 10. The minimum required energy for the ions to execute an orbit taking them across the separatrix decreases as they flow radially outwards. The counter-current directed ions consistently require the lowest surface minimum energy for loss from all the flux surfaces, which is consistent with what was found for the first flux surface.

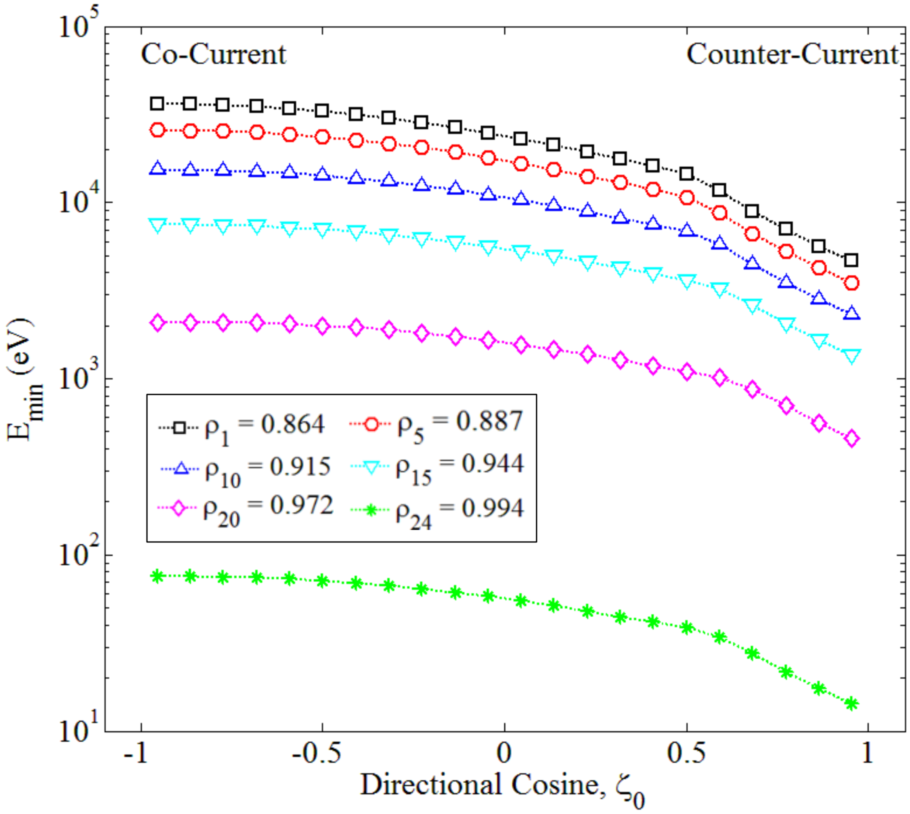

Figure 10. Lowest value of $E_{lowest\ min}(\zeta_0, \rho_k)$ for any launch location ($\theta_0$) on surface ($\rho_k$), at the radial positions: $\rho_1$ = 0.864, $\rho_5$ = 0.887, $\rho_{10}$ = 0.915, $\rho_{15}$ = 0.944, $\rho_{20}$ = 0.972, $\rho_{24}$ = 0.994.

The results shown in Figures 5-10 can be used to calculate a loss region in velocity space that increases with flux surface radius. The velocity loss region may be combined with an approximation of the particle distribution function in velocity space to allow us to calculate a particle loss rate. We assume that the ion velocity distribution function is a Maxwellian at the local ion temperature, chopped off above the local $E_{min}(\zeta_0, \rho)$. By using the directional cosine, $\zeta_0 = \cos(\alpha)$ as derived in Appendix A, given by the azimuthal angle, $\alpha$, between the initial ion velocity, $\vartheta(V_0, \alpha)$, and the toroidal magnetic field, $B_\varphi$, then the differential volume element in spherical velocity space is $(V_0 d\alpha)(2\pi V_0 \sin(\alpha))dV_0 = 2\pi {V_0}^2 dV_0 d\zeta_0$. The number of ions lost within a given $d\alpha$ about a given $\alpha$ is the number within $d\alpha$ with a magnitude of velocity $V_0 \geq V_{0\,min}(\zeta_0)$. For ions in a velocity distribution given by $f(V_0)$, then the number of ions within $d\alpha$ about a given $\alpha$ which are lost is $dN_{loss}(\alpha) = 2\pi \sin(\alpha) \int_{V_{0\,min}(\alpha)}^{\infty} {V_0}^2 f(V_0) dV_0 d\alpha$ and the numbers of ions within $d\zeta_0$ lost is $dN_{loss}(\zeta_0) = d\zeta_0 \int_{V_{0\,min}(\zeta_0)}^{\infty} {V_0}^2 f(V_0) dV_0$.

We assume no scattering between directional bins, so each direction has a Maxwellian distribution at the local ion temperature with an upper cut-off energy corresponding to $V_{0min}(\zeta_0)$, which determines the loss fraction in that direction $\zeta_0$, $dN_{loss}(\zeta_0) = d\zeta_0 \int_{V_{min}(\zeta_0)}^{\infty} V^2 f(V) dV$. The total loss rate from a flux surface for ions which escape across the separatrix is found by integrating $dN_{loss}(\zeta_0)$ over $1 \geq \zeta_0 \geq -1$, $N_{loss} = 2\pi \int_{-1}^{1} \left[ \int_{V_{0\,min}(\zeta_0)}^{\infty} {V_0}^2 f(V_0) dV_0 \right] d\zeta_0 = 2\pi \int_{-1}^{1} \left[ \int_{\varepsilon_{min}(\zeta_0)}^{\infty} \varepsilon^{1/2} e^{-(\varepsilon)} d\varepsilon \right] d\zeta_0$, where $\varepsilon = \frac{1/2 m {V_0}^2}{kT_{ion}}$. The total number of ions on a flux surface in the absence of loss would be $N_{tot} = 2\pi \int_{-1}^{1} d\zeta_0 \int_{0}^{\infty} {V_0}^2 f(V_0) dV_0 = 2\pi \int_{-1}^{1} d\zeta_0 \int_{\varepsilon_{min(\zeta_0)}}^{\infty} \varepsilon^{1/2} e^{-(\varepsilon)} d\varepsilon$.

# Energy Distribution Function

Based on these calculations we make a few generalizations about the energy distribution as a function of direction and flux surface for the radially outward flowing ion flux as a result of IOL. Out to a certain radius (we assume this is at $\rho_{min}$ = $\rho_1$ = 0.864) the minimum required energies $E_{min}(\zeta_0, \theta_S, \theta_0, \rho_0)$ for IOL to occur are so large that few ions can meet the energetic requirements regardless of their direction. Based on the relative difference between the ion poloidal motion and radial transport speeds we assume the ions pass through all poloidal loss locations ($\theta_0$ = 0, ±π/4, ±π/2, ±3π/4 and π) many times in the time required to be transported radially across flux surfaces. So all ions in the radial range $\rho_{\min} \leq \rho \leq \rho_{\min} + \Delta\rho_1$ with energy in the range $E_{min}(\zeta_0, \theta_S, \theta_0, \rho_{\min}) \geq E \geq E_{min}(\zeta_0, \theta_S, \theta_0, \rho_{\min} + \Delta\rho_1)$ dependent upon their directional bin $\zeta_0$ are lost (the fraction of such loss ions is different for the different directional bins $\zeta_0$). For the next radial range $\rho_{\min} + \Delta\rho_1 \leq \rho \leq \rho_{\min} + \Delta\rho_1 + \Delta\rho_2$ those ions in the directional bin $\zeta_0$ with energy in the range $E_{min}(\zeta_0, \theta_S, \theta_0, \rho_{\min} + \Delta\rho_1) \geq E \geq E_{min}(\zeta_0, \theta_S, \theta_0, \rho_{\min} + \Delta\rho_1 + \Delta\rho_2)$ are lost. We continue this process for each directional bin $\zeta_0$ from (-1 $\leq \zeta_0 \leq$ 1) and for each radius from $\rho_1$ = 0.864 out to $\rho$ = 1.0.

The energy distribution for the outward flowing ion flux, for ions of a given directional cosine $\zeta_0$, is a continuously decreasing upper energy limit as the radius increases due to the effects of IOL. The ions with energy above the surface minimums $E_{lowest\ min}(\zeta_0, \rho_1 = 0.864)$ at the first flux surface we investigate ($\rho_1$ = 0.864) would all be lost. For the next flux surface ($\rho_2$ = 0.870) the energy distribution function would start already chopped off above the energy $E_{lowest\ min}(\zeta_0, \rho_1 = 0.864)$ and the ions between this cut-off energy and $E_{lowest\ min}(\zeta_0, \rho_2 = 0.870)$ would then be lost. This procedure is followed for all the remaining flux surfaces for each of the directional cosine bins so that the energy distribution function, in each direction, would be chopped off at the energy $E_{lowest\ min}(\zeta_0, \rho_{k-1})$ all the way out to $\rho$ = 1.0. The ions not lost before reaching $\rho$ = 1.0 are determined by integrating over the energy distribution function chopped off at $E_{lowest\ min}(\zeta_0, \rho_{24})$ from the last flux surface.

The minimum energy for IOL of ions with direction cosine ($\zeta_0$) as a function of flux suface position after these chopping steps are performed on the energy distribution function for each directional cosine on each flux surface is shown as a histogram in Figure 11. The counter-current ions have dramatically lower minimum energy requirements even at the first flux surface resulting in few non-lost ions, while the the non-lost co-current ions have almost the same amount left on their seventeenth surface.

Following a derivation similar to that for the ion loss leads to an expression for the energy and momentum losses and totals [10], where $\varepsilon = \frac{1/2mV_0{}^2}{kT_{ion}}$. $M_{loss} =$

$$2\pi \int_{-1}^{1} \left[\int_{V_{0\,min}(\zeta_0)}^{\infty} (mV_0\zeta_0)V_0{}^2 f(V_0)dV_0\right] d\zeta_0$$

$$= 2\pi \int_{-1}^{1} \left[\zeta_0 \int_{\varepsilon_{min(\zeta_0)}}^{\infty} \varepsilon e^{-(\varepsilon)} d\varepsilon\right] d\zeta_0 \quad (9)$$

$$M_{tot} = 2\pi \int_{-1}^{1} d\zeta_0 \int_0^{\infty} (mV_0)V_0{}^2 f(V_0)dV_0 = 2\pi \int_{-1}^{1} d\zeta_0 \int_{\varepsilon_{min(\zeta_0)}}^{\infty} \varepsilon e^{-(\varepsilon)} d\varepsilon \quad (10)$$

$$E_{loss} = 2\pi \int_{-1}^{1} \left[\int_{V_{0\,min}(\zeta_0)}^{\infty} \left(\frac{1}{2}mV_0{}^2\right) V_0{}^2 f(V_0)dV_0\right] d\zeta_0$$

$$= 2\pi \int_{-1}^{1} \left[\int_{\varepsilon_{min(\zeta_0)}}^{\infty} \varepsilon^{3/2} e^{(-\varepsilon)} d\varepsilon\right] d\zeta_0 \quad (11)$$

$$E_{tot} = 2\pi \int_{-1}^{1} d\zeta_0 \int_0^{\infty} \left(\frac{1}{2}mV_0{}^2\right) V_0{}^2 f(V_0)dV_0 = 2\pi \int_{-1}^{1} d\zeta_0 \int_{\varepsilon_{min(\zeta_0)}}^{\infty} \varepsilon^{3/2} e^{(-\varepsilon)} d\varepsilon \quad (12)$$

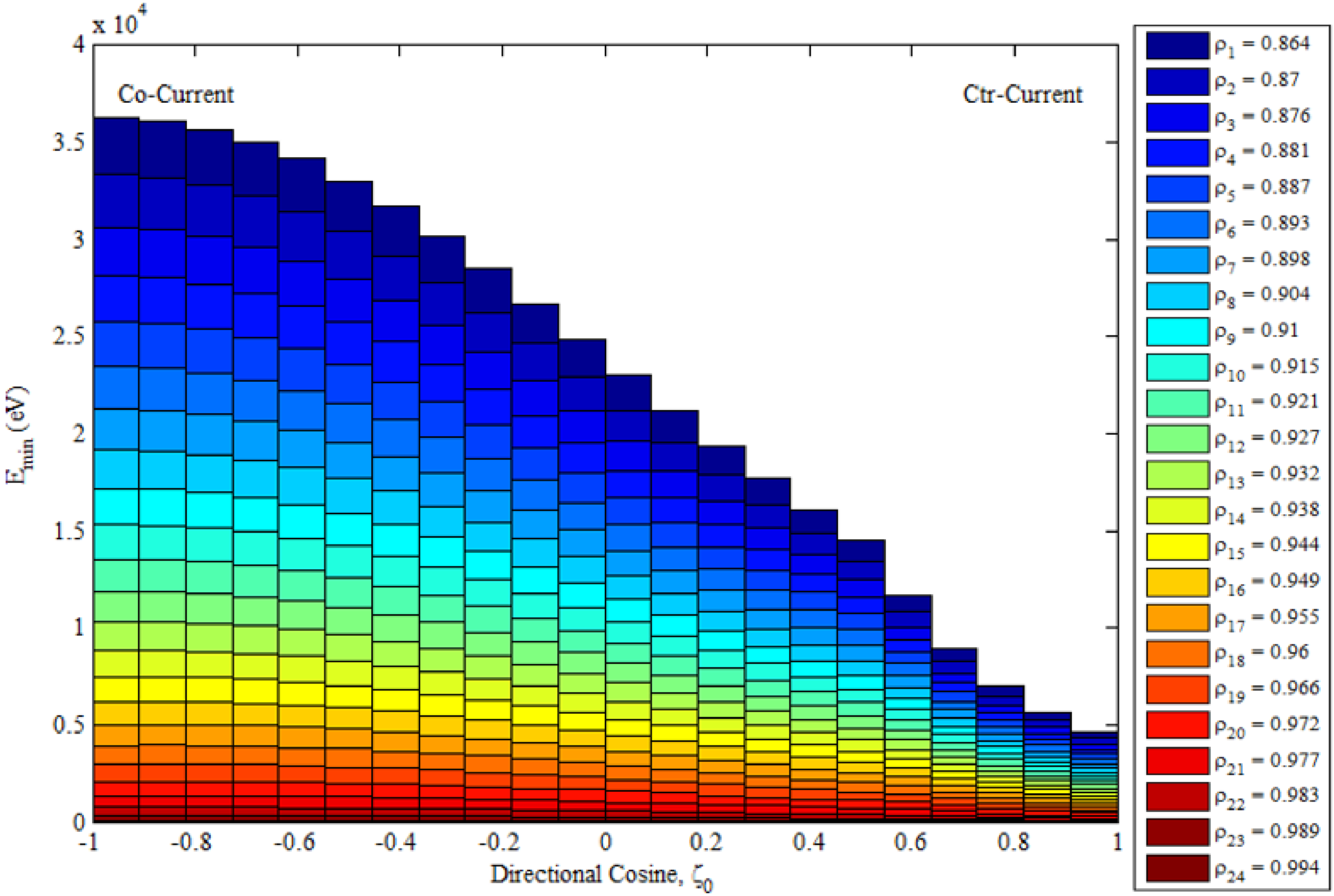

Figure 11. Minimum energy for ion orbit loss of ions with direction cosine ($\zeta_0$) as a function of radial flux surface ($\rho_k$).

# CHAPTER 4
# ION-ORBIT-LOSS ESCAPE FRACTIONS AND ALLOCATIONS

## Escape Fractions

We can evaluate the integrals of the previous chapter total and ion-orbit-lost particles, momentum and energy, in terms of the complete and incomplete gamma functions [10]

$$\Gamma(a) = \int_0^{\infty} \varepsilon^{a-1} e^{-\varepsilon} d\varepsilon, \tag{13a}$$

$$\Gamma(a,x) = \int_x^{\infty} \varepsilon^{a-1} e^{-\varepsilon} d\varepsilon, \tag{13b}$$

$$\gamma(a,x) = \int_0^{x} \varepsilon^{a-1} e^{-\varepsilon} d\varepsilon, \tag{14}$$

when a Maxwellian distribution is used, where now $a = \frac{3}{2}, \frac{4}{2}, \frac{5}{2}$ for ion, momentum, and energy integrals, respectively.

At the innermost radius ($\rho_1$= 0.864) at which ion orbit loss is important, we treat the ion distribution as isotropic in direction and Maxwellian in energy. As discussed in Appendix A, a solid angle sampling factor $f(\zeta_i)$ may be used to represent the fraction of the total solid angle contained within each directional cosine bin $\zeta_0$ (this removes the need for the factor of 2 in the total loss for ion, momentum and energy). Due to our uniform sampling of the directional cosine, the factor $f(\zeta_i)$ is a constant 1/22 for each directional cosine bin. Using the ion fraction and total with Equations (13) and (14) , the solid angle sampling factor $f(\zeta_i)$, and the minimum reduced energy from Equation (8) we find the definition for the differential loss fractions for all launch and exit locations and directional cosine bins on the first flux surface ($\rho_1$ = 0.864) for ions, where $\varepsilon = \frac{1/2 m {V_0}^2}{kT_{ion}}$.

$$\frac{N_{loss}}{N_{tot}} = \frac{\left[\int_0^\infty \varepsilon^{1/2} EXP(-\varepsilon)d\varepsilon - \int_0^{\varepsilon_{min}(\zeta_0,\theta_S,\theta_0,\rho_1)} \varepsilon^{1/2} EXP(-\varepsilon)d\varepsilon\right]*f(\zeta_0)}{\int_0^\infty \varepsilon^{1/2} EXP(-\varepsilon)d\varepsilon} =$$

$$\frac{\int_{\varepsilon_{min}(\zeta_0,\theta_S,\theta_0,\rho_1)}^\infty \varepsilon^{1/2} EXP(-\varepsilon)d\varepsilon * f(\zeta_0)}{\int_0^\infty \varepsilon^{1/2} EXP(-\varepsilon)d\varepsilon}$$

We designate these as “un-allocated” (UA) differential ion loss fractions from the given flux surface

$$\text{UA\_}\Delta F_{loss}(\zeta_0,\theta_S,\theta_0,\rho_1) = \frac{N_{loss}}{N_{tot}} = \frac{\Gamma\left(3/2,\varepsilon_{min}(\zeta_0,\theta_S,\theta_0,\rho_1)\right)*\frac{1}{22}}{\Gamma(3/2)} \qquad \text{(15a)}$$

Similar “un-allocated” momentum and energy loss fractions are likewise defined

$$\text{UA\_}\Delta M_{loss}(\zeta_0,\theta_S,\theta_0,\rho_1) = \frac{M_{loss}}{M_{tot}} = \frac{\zeta_0 \int_{\varepsilon_{min}(\zeta_0,\theta_S,\theta_0,\rho_1)}^\infty \varepsilon EXP(-\varepsilon)d\varepsilon * f(\zeta_0)}{\int_0^\infty \varepsilon EXP(-\varepsilon)d\varepsilon} =$$

$$\frac{\zeta_0 \Gamma\left(4/2,\varepsilon_{min}(\zeta_0,\theta_S,\theta_0,\rho_1)\right)*\frac{1}{22}}{\Gamma(4/2)}, \qquad \text{(15b)}$$

and

$$\text{UA\_}\Delta E_{loss}(\zeta_0,\theta_S,\theta_0,\rho_1) = \frac{E_{loss}}{E_{tot}} = \frac{\int_{\varepsilon_{min}(\zeta_0,\theta_S,\theta_0,\rho_1)}^\infty \varepsilon^{3/2} EXP(-\varepsilon)d\varepsilon * f(\zeta_0)}{\int_0^\infty \varepsilon^{3/2} EXP(-\varepsilon)d\varepsilon} =$$

$$\frac{\Gamma\left(5/2,\varepsilon_{min}(\zeta_0,\theta_S,\theta_0,\rho_1)\right)*\frac{1}{22}}{\Gamma(5/2)}. \qquad \text{(15c)}$$

These fractions are designated “un-allocated” because we have not yet specified how ion, momentum or energy from a given location on an inner flux surface that could energetically (i.e. while satisfying Equations 1, 2 and 4) exit at multiple locations on the separatrix are to be allocated among these multiple locations. We next address this issue.

## Poloidal Allocation Methodology

### Poloidal Exit Location Allocation

To calculate the full differential loss fractions for ions, energy and momentum we need to understand where these various fluxes are permitted to go poloidally. We assume that the outward ion flux, from the first flux surface for which ion orbit loss is important ($\rho_1$ = 0.864), is isotropically distributed in direction and uniform in poloidal distribution over the flux surface. The outward radial ion flux reaching each flux surface is evenly distributed among the eight octants centered on the eight poloidal launch locations ($\theta_0$ = π, ±3π/4, ±π/2, ±π/4 and 0) so an eighth of the ions go to each of the poloidal launch locations within each direction for each flux surface. For example, in Figure 12 we took the ions in the Maxwellian energy distribution with the flux surface ($\rho_1$ = 0.864) local ion temperature in the directional bin centered on $\zeta_0$ = 0.955 and placed a distribution of the same shape but at 1/8th of the total flux magnitude at each of the eight poloidal launch locations $\theta_0$ = π, ±3π/4, ±π/2, ±π/4 and 0.

Our method does not involve particle tracking so we only know whether or not an ion has enough energy to reach a given exit location, not that it will go there without having first passed through another energetically allowed exit location. However, knowledge of the minimum required energy to reach each exit location from each launch location, along with the assumed Maxwellian ion energy distribution function, may be used to develop an approximation in place of the calculationally intensive particle following method. From Figure 12 we can use Equation (8) to calculate the minimum energy an ion with directional cosine $\zeta_0$ = 0.955 must possess at each of the eight poloidal launch locations ($\theta_0$) in order to exit the separatrix at each of the eight poloidal exit locations ($\theta_S$) on the separatrix, see Figure 13.

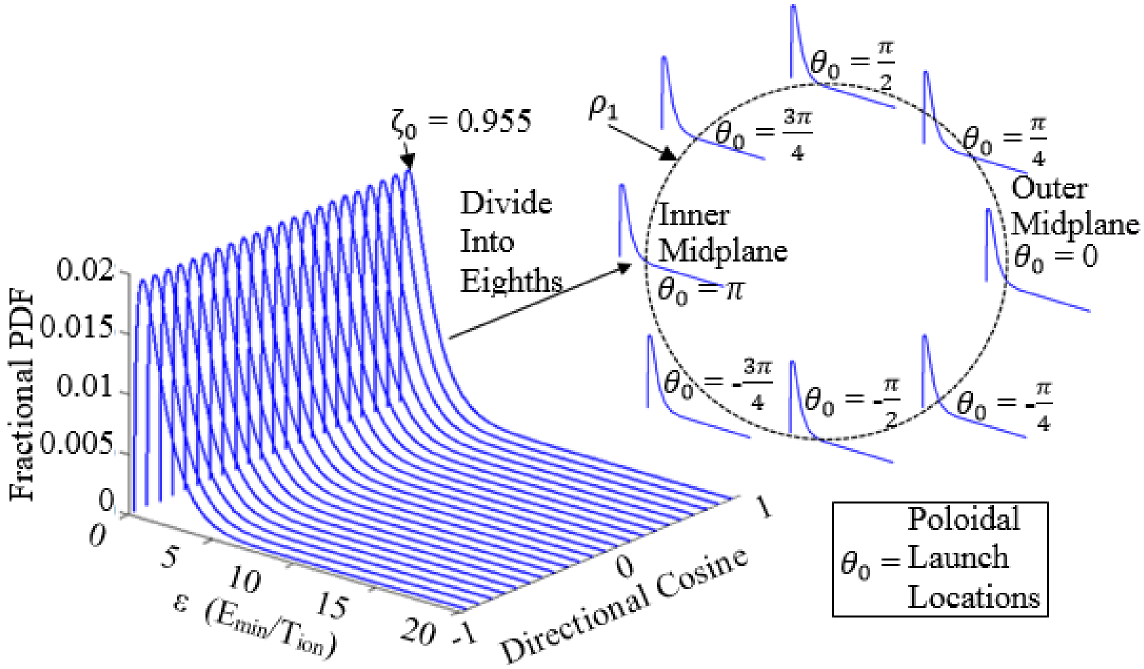

Figure 12. Initial even distribution of ions from the $\zeta_0$ = 0.955 directional cosine bin on the first internal flux surface to the eight poloidal launch locations.

With the known minimum required energies $E_{min}(\zeta_0, \theta_S, \theta_0, \rho_0)$ we can devise an algorithm for making the allocation over the poloidal exit locations ($\theta_S$) on the separatrix ($\rho_S$). For the ions located at the poloidal launch position on the first flux surface ($\rho_1$ = 0.864) at the inner midplane ($\theta_0$ = $\pi$) the corresponding minimum required energies to stream along an orbit out to various poloidal exit points on the separatrix can be found in the dashed green oval on Figure 13. For the selected points the poloidal exit location at the outer midplane ($\theta_S$ = 0 = 2$\pi$), black square in Figure 13, has the lowest minimum energy requirement while the inner midplane ($\theta_S$ = $\pi$), left facing magenta triangle in Figure 13, has the highest.

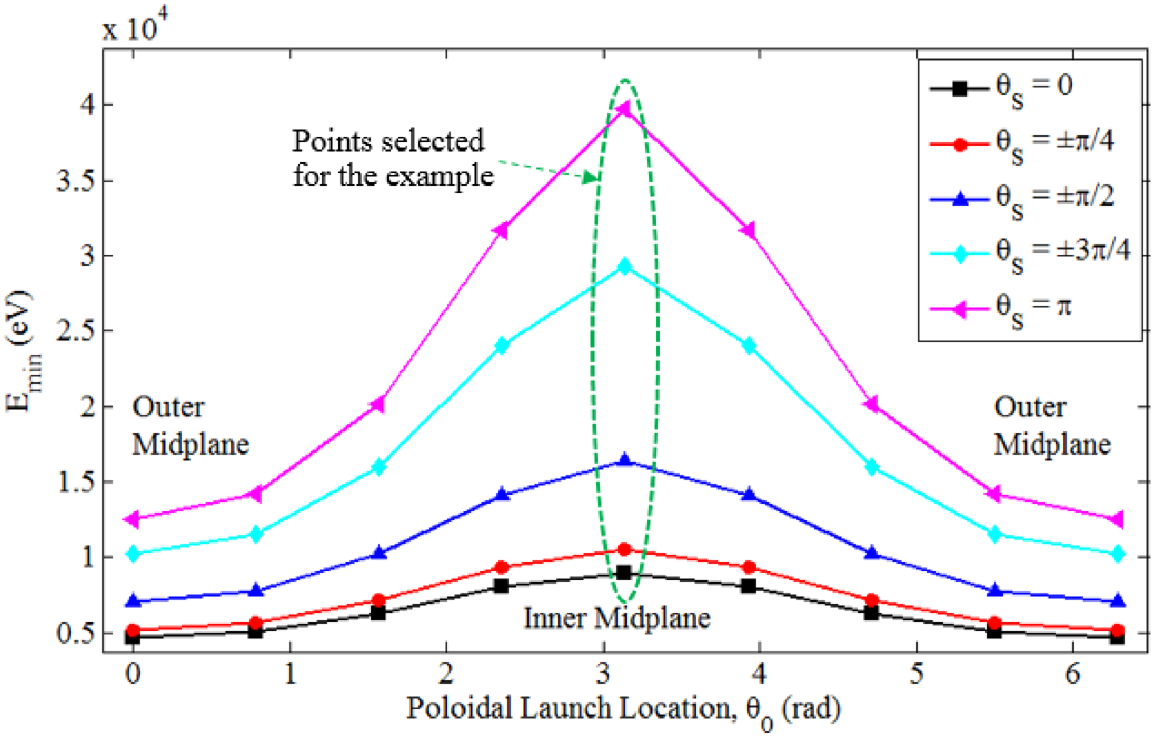

Figure 13. Minimum energy in the $\zeta_0$ = 0.955 (counter-current) directional cosine bin for each of the eight launch positions ($\theta_0$) on the first flux surface ($\rho_1$ = 0.864) required to reach each poloidal exit location ($\theta_S$) on the separatrix ($\rho_S$).

The relative number of ions which meet the energetic requirements demanded by Equation (15) for the selected points are shown in Figure 14. The poloidal exit position on the outer midplane ($\theta_S = 0 = 2\pi$) has the lowest required minimum energy, resulting in the largest number of available ions which can meet this energetic requirement. The poloidal exit position on the inner midplane ($\theta_S = \pi$) results in the smallest number of availible ions which meet this energtic requirement.

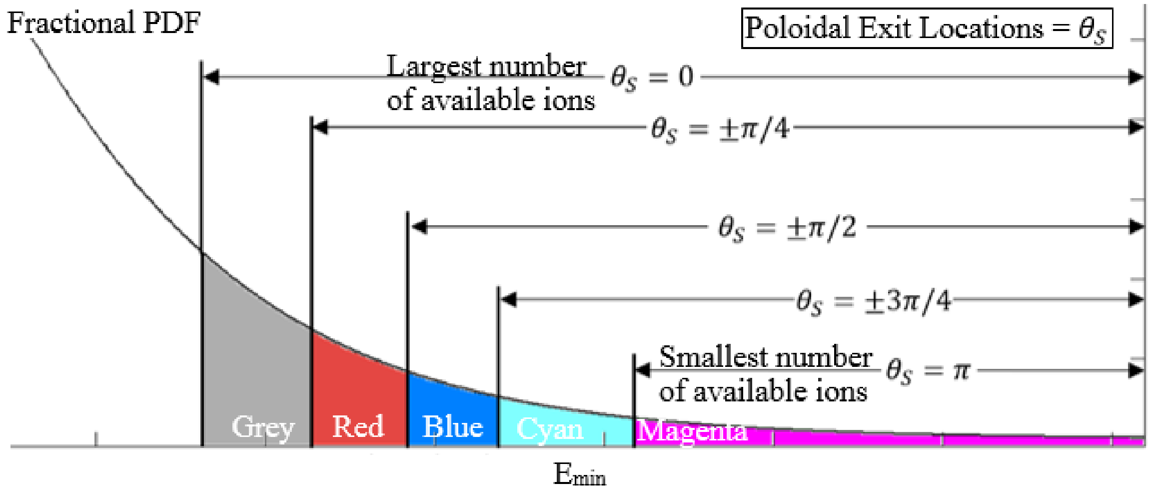

Figure 14. Allowable energy ranges (not to scale) for the example poloidal exit positions ($\theta_S$) as selected from the green oval in Figure 13.

All of the ions contained in the energy range corresponding to an orbit exiting at the inner midplane $\theta_S = \pi$ (magenta colored region in Figure 14) on the separatrix $\rho_S$ also have enough energy to execute an orbit taking them to any of the other poloidal exit locations $\theta_S = \pm3\pi/4, \pm\pi/2, \pm\pi/4$ and 0, eight in total. The ions in the energy range from $\theta_S = \pm3\pi/4$ to $\theta_S = \pi$ (cyan colored region in Figure 14) have enough energy to execute orbits exiting at $\theta_S = \pm3\pi/4, \pm\pi/2, \pm\pi/4$ and 0, seven in total. We count the number of energetically allowable exit locations for each energy range until the last energy range between $\theta_S = 0$ and $\theta_S = \pm\pi/4$ (grey colored region in Figure 14) which contains ions only having enough energy to make it to one location on the outer midplane, $\theta_S = 0$.

We assume that the ions from each launch location are distributed evenly among all the energetically allowed exit locations. The ion loss fraction, from Equation (15), for the ions which have enough energy to exit at the poloidal location $\theta_S = \pi$ (magenta energy region in Figure 14) is divided by the number of energetically allowable exit locations $\frac{\text{UA\_}\Delta F_{loss}(\zeta_0=0.955,\theta_S=\pi,\theta_0=\pi,\rho_1=0.864)}{8}$ and allocated evenly over all eight exit locations.

Similarly, the ion loss fraction representing the ions within the energy range from $\theta_S$ = ±3π/4 to $\theta_S$ = π (cyan energy range in Figure 14) is divided by seven $\frac{\mathrm{UA\_}\Delta F_{loss}(\zeta_0=0.955,\theta_S=\pm 3\pi/4,\theta_0=\pi,\rho_1=0.864)}{7}$ and allocated equally to all the $\theta_S$ locations which are energetically allowed. We continue applying this allocation process until the energy range between $\theta_S$ = 0 and $\theta_S$ = ±π/4 (grey colored region in Figure 14). These ions are only lost to the poloidal exit location $\theta_S = 0$ as it is the only exit location on the separatrix they have enough energy to execute an orbit to. The fractional values of the energy ranges from Figure 14 as well as the ion loss fractional values at each poloidal exit location after application of this allocation method are provided in Table 1.

The other seven poloidal launch locations $\theta_0$ = ±3π/4, ±π/2, ±π/4 and 0, are allocated over their poloidal exit locations with the same method as in the example. The general allocation method for exit locations is performed as follows. We calculate the un-allocated loss fraction for each poloidal exit location by using the minimum required energy $E_{min}(\zeta_0, \theta_S, \theta_0, \rho_0)$ for each poloidal exit location in Equation (15). Then we sort the minimum required energy $E_{min}(\zeta_0, \theta_S, \theta_0, \rho_0)$ for each poloidal exit location to establish energy range bins. Next, we divide the un-allocated loss fraction by the number of energetically allowed exit locations and allocate them to the proper poloidal exit location $\theta_S$. These allocations are summed for the total fraction of ions which we estimate at each poloidal exit location $\theta_S$ on the separatrix $\rho_S$ from a given poloidal launch location $\theta_0$ in some inner flux surface $\rho_0$.

Table 1. Fractional values of the various colored energy ranges in Figure 14 as well as the resulting fractional values at each poloidal exit location $\theta_S$.

| **Energy Region** | **Magenta**<br>$\theta_S = \pi$ to $\infty$ | **Cyan**<br>$\theta_S = \pm 3\pi/4$ to $\pi$ | **Blue**<br>$\theta_S = \pm\pi/2$ to $\pm 3\pi/4$ | **Red**<br>$\theta_S = \pm\pi/4$ to $\pm\pi/2$ | **Grey**<br>$\theta_S = \pm\pi/2$ to 0 |
|---|---|---|---|---|---|
| **Un-Allocated Loss Fraction of Ions ($10^{-4}$)** | 2.133E-11 | 9.268E-08 | 2.060E-03 | 1.462E-01 | 2.767E-01 |
| **# of Energetically Allowed Exit Locations** | 8 | 7 | 5 | 3 | 1 |

| **Poloidal Exit Locations on the Separatrix** | $\theta_S = \pi$ | $\theta_S = \pm 3\pi/4$ | $\theta_S = \pm\pi/2$ | $\theta_S = \pm\pi/4$ | $\theta_S = 0$ |
|---|---|---|---|---|---|
| **From Magenta Energy Region ($10^{-4}$)** | 2.666E-12 | 2.666E-12 | 2.666E-12 | 2.666E-12 | 2.666E-12 |
| **From Cyan Energy Region ($10^{-4}$)** | 0 | 1.324E-08 | 1.324E-08 | 1.324E-08 | 1.324E-08 |
| **From Blue Energy Region ($10^{-4}$)** | 0 | 0 | 4.120E-04 | 4.120E-04 | 4.120E-04 |
| **From Red Energy Region ($10^{-4}$)** | 0 | 0 | 0 | 4.875E-02 | 4.875E-02 |
| **From Grey Energy Region ($10^{-4}$)** | 0 | 0 | 0 | 0 | 2.767E-01 |
| **Allocated Totals ($10^{-4}$)** | 2.666E-12 | 1.324E-08 | 4.120E-04 | 4.916E-02 | 3.259E-01 |

## Poloidal Launch Location Allocation

All of the ions which are physically capable of being lost to the poloidal exit locations on the separatrix from each poloidal launch location on an inner flux surface are assumed to be lost immediately. However, each poloidal launch location has different minimum energies required to reach the various poloidal exit locations on the separatrix, see Figure 13. Due to this differenece the energy range, and number, of the non-lost ions will be different for each poloidal launch position ($\theta_0$) in a given directional cosine ($\zeta_0$ = 0.955 for our example). The $\theta_S$ = 0 poloidal exit location has the lowest minimum required energy for each poloidal launch location ($\theta_0$) so we may use this minimum curve to set the upper limit of the expected energy of the non-lost ions at each poloidal launch position (this corresponds to the black squares curve in Figure 13).

Ions exist at these different poloidal launch locations which could be lost from other poloidal launch locations. The ions spiral about the flux surface many times before they move radially to the next flux surface, so they are able to reach the other poloidal launch locations where they can then be lost. These ions also have a preferential poloidal spiral direction about the flux surface which is determined by the orientation of the ion guiding center velocity relative to the toroidal current $I$ and magnetic field $B_\varphi$, recall Figure 1. Ions, for this tokamak shot, moving in the co-current direction ($\zeta_0 < 0$) spiral poloidally about their flux surface counter clock-wise while ions moving in the counter-current direction ($\zeta_0 > 0$) spiral poloidally about the flux surface in the clock-wise direction, see Figure 15.

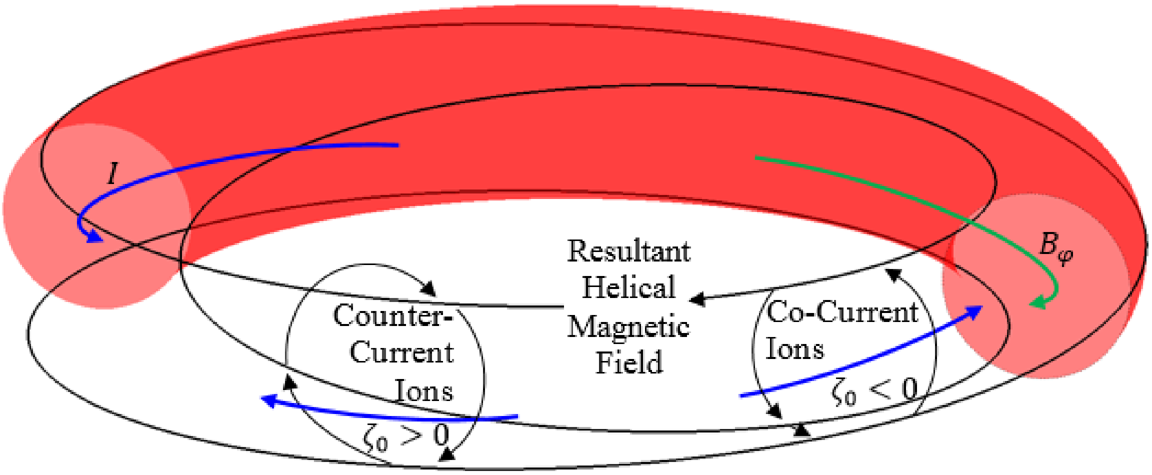

Figure 15. Toroidal ion directions shown with the resultant helical magnetic field also describing intra-flux surface poloidal motion directions.

To account for this intra-flux surface poloidal ion motion we perform a secondary allocation over the poloidal launch positions ($\theta_0$). Using the energy curve from our example in Figure 15 with Equation (17) we can find the loss fraction from each poloidal launch position ($\theta_0 = \pm 3\pi/4, \pm\pi/2, \pm\pi/4$ and 0), see Figure 17. The ions at the inner midplane ($\theta_0 = \pi$) are assumed to be immediately lost in the magenta energy region of Figure 17. These ions are solely lost from the poloidal launch position $\theta_0 = \pi$ to the various poloidal exit positions $\theta_S$ on the separatrix and the loss fractions are allocated according to the method described in the previous section.

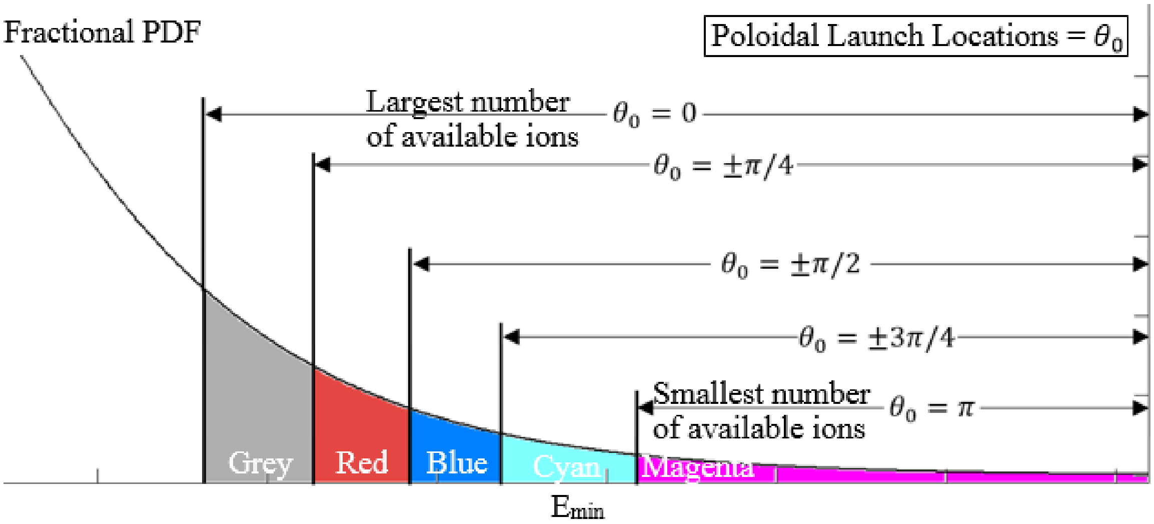

Figure 16. Allowable energy ranges (not to scale) for the example poloidal launch positions ($\theta_0$), from the black squares curve Figure 13.

Our example case deals with ions in a directional cosine bin pointing in the counter-current direction $\zeta_0 > 0$ so the remaining non-lost ions will move clock-wise poloidally. The non-lost ions at $\theta_0 = \pi$ (the grey through cyan energy ranges in Figure 17) will spiral clock-wise poloidally to the next position, see Figure 18. At the next position $\theta_0 = +3\pi/4$ the ions which meet the physical requirements for loss at $\theta_0 = +3\pi/4$ (the cyan energy range in Figure 17) will be immediately lost and the corresponding loss fraction for the cyan region will be allocated in the manner described in the previous section, see Figure 18. The non-lost ions from $\theta_0 = \pi$ will continue to move clock-wise poloidally to the $\theta_0 = +\pi/2$ poloidal launch position at the top of the flux surface, where the ions in the blue energy range in Figure 17 will be lost and fractions allocated accordingly. We continue this process until the reamaining non-lost ions reach the outer midplane at $\theta_0 = 0$ where the grey energy region of ions from Figure 17 will be lost, and the corresponding remaining loss fraction is allocated accordingly.

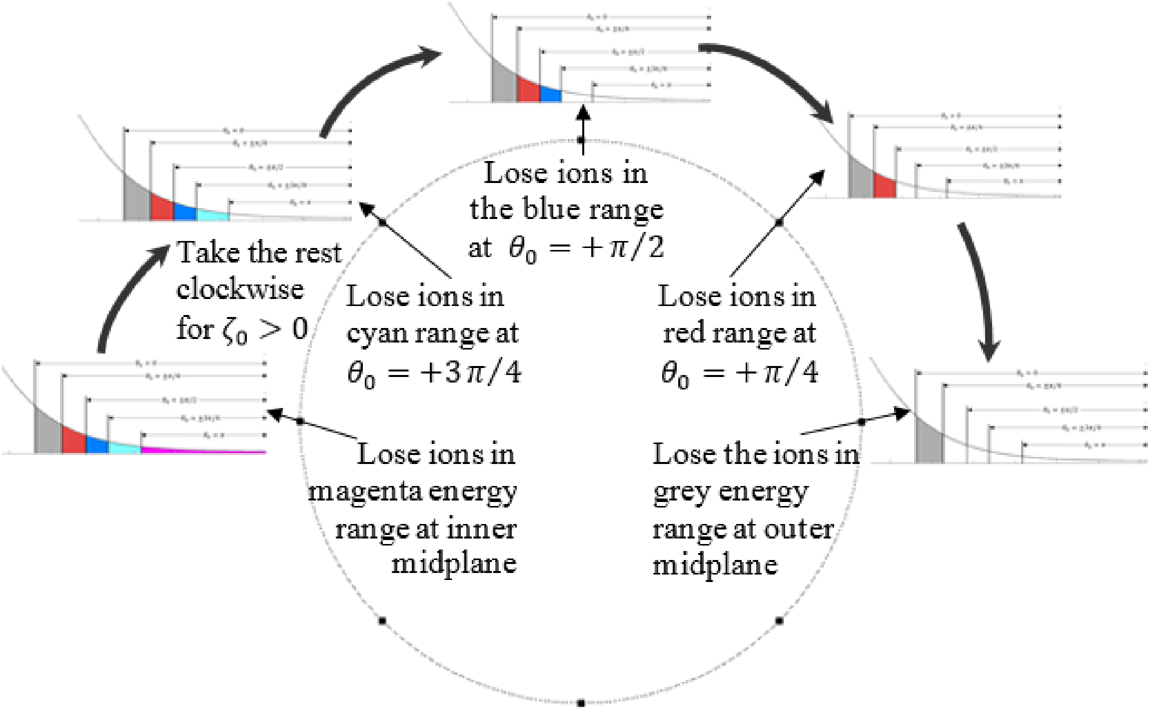

Figure 17. Poloidal launch location ($\theta_0$) allocation method for a positive directional cosine case ($\zeta_0 > 0$) starting at $\theta_0$ = π. The rotating distribution is taken directly from Figure 16.

The ions at the other poloidal launch positions $\theta_0$ = ±3π/4, ±π/2, ±π/4, 0 on the flux surface $\rho_1$ = 0.864 within the directional cosine bin $\zeta_0$ = 0.955 will be allocated in the same manner as the example. The ions will be allocated over the poloidal exit locations $\theta_s$ for which they meet the energetic requirements as described in the previous section. Any remaining ions will spiral poloidally in the clock-wise direction to the poloidal locations $\theta_{0,\varepsilon_{min}\,lower}$ with lower minimum energy requirements $E_{min}\big(\zeta_0 = 0.955, \theta_S, \theta_{0,E_{min}\,lower}, \rho_1 = 0.864\big) < E_{min}(\zeta_0 = 0.955, \theta_S, \theta_0, \rho_1 = 0.864)$ to execute orbits which reach the separatrix where they are lost. At the end of the allocation process for the example case all of the non-lost ions have energies below the surface minimum energy $E_{lowest\ min}(\zeta_0 = 0.955, \rho_1)$. The ions in the other directional cosine bins in the counter-current direction $0.955 > \zeta_0 > 0$ will also be allocated by this same method.

For the ions in co-current directional bins $0 > \zeta_0 > -1$ both allocation processes will be identical with only one exception. The ions will spiral in the poloidal counter clock-wise direction when moving from a poloidal launch location with high overall minimum energy with respect to one with lower overall minimum energy $E_{min}\left(\zeta_0 < 0, \theta_S, \theta_{0,E_{min}\ lower}, \rho_0 = 0.864\right) < E_{min}(\zeta_0 < 0, \theta_S, \theta_0, \rho_1 = 0.864)$. The ion, energy and momentum loss fractions for the first flux surface will be calculated using Equation (15) and allocated over poloidal exit and launch positions as described in these allocation sections.

## Loss Fractions Beyond the First Flux Surface

Once the allocation over poloidal exit $\theta_S$ and poloidal launch $\theta_0$ locations is completed for each directional cosine $\zeta_0$ on the first flux surface $\rho_1$ = 0.864 we generate the loss fractions for the next flux surface and allocate them accordingly. However, each flux surface, beyond the first one we evaluate, has a truncated or 'chopped' energy distribution due to the ions lost on the previous flux surface(s). All directional cosine bins within each flux surface beyond the first, $\rho_k$ where $k > 1$, will contain energy distributions which only include those ions with energies below the surface minimum from the previous flux surface $E_{cut}(\zeta_0, \rho_{\mathrm{k}-1})$ for that directional cosine bin. This 'cutting energy' is synonymons the with $E_{lowest\,min}(\zeta_0, \rho_{k-1})$ we introdued in chapter 3. We can use these overall minimums to cut or truncate the energy distributions used in Equation (15) for ions, where $\varepsilon = \frac{1/2mV_0{}^2}{kT_{ion}}$

$$N_{loss} = \left[\int_{\varepsilon_{min}(\zeta_0,\theta_S,\theta_0,\rho_k)}^{\infty} \left(\frac{2kT}{m}\right)^{1/2} EXP\left(-\left(\varepsilon\frac{2kT}{m}\right)\right) d\varepsilon - \right.$$

$$\left. \int_{\varepsilon_{cut}(\zeta_0,\rho_{\mathrm{k}-1})}^{\infty} \left(\varepsilon\frac{2kT}{m}\right)^{1/2} EXP\left(-\left(\varepsilon\frac{2kT}{m}\right)\right) d\varepsilon\right], \tag{16}$$

in Equation (11) for momentum,

$$M_{loss} = \left[\int_{\varepsilon_{min}(\zeta_0,\theta_S,\theta_0,\rho_k)}^{\infty} \left(\varepsilon\frac{2kT}{m}\right)^{2/2} EXP\left(-\left(\varepsilon\frac{2kT}{m}\right)\right) d\varepsilon - \right.$$

$$\left. \int_{\varepsilon_{cut}(\zeta_0,\rho_{\mathrm{k}-1})}^{\infty} \left(\varepsilon\frac{2kT}{m}\right)^{2/2} EXP\left(-\left(\varepsilon\frac{2kT}{m}\right)\right) d\varepsilon\right], \tag{17}$$

and in Equation (13) for energy,

$$E_{loss} = \left[\int_{\varepsilon_{min}(\zeta_0,\theta_S,\theta_0,\rho_k)}^{\infty} \left(\varepsilon \frac{2kT}{m}\right)^{3/2} EXP\left(-\left(\varepsilon \frac{2kT}{m}\right)\right) d\varepsilon - \int_{\varepsilon_{cut}(\zeta_0,\rho_{\mathrm{k}-1})}^{\infty} \left(\varepsilon \frac{2kT}{m}\right)^{3/2} EXP\left(-\left(\varepsilon \frac{2kT}{m}\right)\right) d\varepsilon\right], \tag{18}$$

where k >1. These loss number equations are used to derive the un-allocated loss fractions for all flux surfaces beyond the first by replacing the loss number equations in the derivation for Equation (15) with Equations (16-18) for ions

$$\mathrm{UA\_}\Delta F_{loss}(\zeta_0, \theta_S, \theta_0, \rho_k) = \frac{N_{loss}}{N_{tot}} =$$

$$\frac{\left[\int_{\varepsilon_{min}(\zeta_0,\theta_S,\theta_0,\rho_k)}^{\infty} \varepsilon^{1/2} EXP(-\varepsilon)d\varepsilon - \int_{\varepsilon_{cut}(\zeta_0,\rho_{\mathrm{k}-1})}^{\infty} \varepsilon^{1/2} EXP(-\varepsilon)d\varepsilon\right] * f(\zeta_0)}{\int_0^{\infty} \varepsilon^{1/2} EXP(-\varepsilon)d\varepsilon} =$$

$$\frac{\left[\Gamma\left(3/2, \varepsilon_{min}(\zeta_0,\theta_S,\theta_0,\rho_{\mathrm{k}})\right) - \Gamma\left(3/2, \varepsilon_{cut}(\zeta_0,\rho_{\mathrm{k}-1})\right)\right] * \frac{1}{22}}{\Gamma(3/2)}, \tag{19a}$$

with Equation (19) for momentum

$$\mathrm{UA\_}\Delta \mathrm{M}_{loss}(\zeta_0, \theta_S, \theta_0, \rho_k) = \frac{M_{loss}}{M_{tot}} =$$

$$\frac{\zeta_0\left[\int_{\varepsilon_{min}(\zeta_0,\theta_S,\theta_0,\rho_k)}^{\infty} \varepsilon EXP(-\varepsilon)d\varepsilon - \int_{\varepsilon_{cut}(\zeta_0,\rho_{\mathrm{k}-1})}^{\infty} \varepsilon EXP(-\varepsilon)d\varepsilon\right] * f(\zeta_0)}{\int_0^{\infty} \varepsilon EXP(-\varepsilon)d\varepsilon} =$$

$$\frac{\zeta_0\left[\Gamma\left(2, \varepsilon_{min}(\zeta_0,\theta_S,\theta_0,\rho_{\mathrm{k}})\right) - \Gamma\left(2, \varepsilon_{cut}(\zeta_0,\rho_{\mathrm{k}-1})\right)\right] * \frac{1}{22}}{\Gamma(2)}, \tag{19b}$$

and with Equation (20) for energy

$$\mathrm{UA\_}\Delta E_{loss}(\zeta_0, \theta_S, \theta_0, \rho_k) = \frac{E_{loss}}{E_{tot}} =$$

$$\frac{\left[\int_{\varepsilon_{min}(\zeta_0,\theta_S,\theta_0,\rho_k)}^{\infty} \varepsilon^{3/2} EXP(-\varepsilon)d\varepsilon - \int_{\varepsilon_{cut}(\zeta_0,\rho_{\mathrm{k}-1})}^{\infty} \varepsilon^{3/2} EXP(-\varepsilon)d\varepsilon\right] * f(\zeta_0)}{\int_0^{\infty} \varepsilon^{3/2} EXP(-\varepsilon)d\varepsilon} =$$

$$\frac{\left[\Gamma\left(5/2, \varepsilon_{min}(\zeta_0,\theta_S,\theta_0,\rho_{\mathrm{k}})\right) - \Gamma\left(5/2, \varepsilon_{cut}(\zeta_0,\rho_{\mathrm{k}-1})\right)\right] * \frac{1}{22}}{\Gamma(5/2)}, \tag{19c}$$

where, where $\varepsilon = \frac{1/2 m {V_0}^2}{kT_{ion}}$ and k >1.

Using Equations (15) and (19) we calculate the un-allocated loss fractions for all flux surfaces $\rho_k$ for $1 \leq k \leq 24$ over all directional cosine bins $(-1 \leq \zeta_0 \leq 1)$. We allocate these loss fractions from all of the poloidal launch locations ($\theta_0$ = π, ±3π/4, ±π/2, ±π/4 and 0) over all the energetically allowable poloidal exit locations ($\theta_S$ = π, ±3π/4, ±π/2, ±π/4 and 0). Any remaining ions which do not meet the energetic requirements at their initial poloidal launch location $\theta_0$ are taken to nearby poloidal launch locations $\theta_{0,\varepsilon_{min}\,lower}$ with lower overall minimum reduced energy requirements $\varepsilon_{min}\left(\zeta_0, \theta_S, \theta_{0,\varepsilon_{min}\,lower}, \rho_0\right) < \varepsilon_{min}(\zeta_0, \theta_S, \theta_0, \rho_0)$. The choice of nearby poloidal launch locations is determined solely by the particular directional cosine bin of the ions. For co-current directed ions $(-1 \leq \zeta_0 < 0)$ the poloidal spiral motion is counter clock-wise while the counter-current directed ions $(0 < \zeta_0 \leq 1)$ the poloidal motion is clock-wise. This allocation is continued until all the non-lost ions in a given directional cosine bin are below the surface minimum energy $E_{lowest\,min}(\zeta_0, \rho_0)$.

All of the fully allocated loss fractions are stored in differential form over the directional cosine ($\zeta_0$) bin to which they belong, the poloidal exit locations ($\theta_S$) on the separatrix ($\rho_S$) they exit at, the poloidal launch locations ($\theta_0$) they are launched from and the inner flux surface radius ($\rho_0$) they were at when their orbit took them out to the separatrix to be lost. These allocated full differential loss fractions for ions, momentum and energy are given by $\Delta F_{loss}(\zeta_0, \theta_S, \theta_0, \rho_0)$, $\Delta M_{loss}(\zeta_0, \theta_S, \theta_0, \rho_0)$ and $\Delta \mathrm{E}_{loss}(\zeta_0, \theta_S, \theta_0, \rho_0)$. We can now sum the full differential loss fractions over any of their four dimensions $\sum_{\zeta_0=1}^{22} \sum_{\theta_S=1}^{8} \sum_{\theta_0=1}^{8} \sum_{k=1}^{24} [\zeta_0, \theta_S, \theta_0, \rho_k]$ to generate a corresponding IOL distribution over the remaining dimensions. Summing the full differential ion loss fraction over the directional cosines $\zeta_0$, poloidal exit locations $\theta_S$, and internal flux surface positions $\rho_0$ will give the ion loss fraction as a distribution over poloidal launch positions (this also applies to the momentum and energy full differential loss fractions)

$$\Delta F_{loss}(\theta_0) = \sum_{\zeta_0=1}^{22} \sum_{\theta_S=1}^{8} \sum_{k=1}^{24} [\Delta F_{loss}(\zeta_0, \theta_S, \theta_0, \rho_k)]. \tag{20}$$

The full differential loss fractions could also be summed over just a few of the dimensions such as the poloidal exit locations $\theta_S$ and internal flux surface positions $\rho_0$ which will yield a distribution of the ion loss fractions over directional cosine and poloidal launch locations

$$\Delta F_{loss}(\zeta_0, \theta_0) = \sum_{\theta_S=1}^{8} \sum_{k=1}^{24} [\Delta F_{loss}(\zeta_0, \theta_S, \theta_0, \rho_k)]. \tag{21}$$

Or the full differential loss fractions could be summed over all of their dimensions to find an overall loss fraction for the whole plasma given by

$$F_{orb} = \sum_{\zeta_0=1}^{22} \sum_{\theta_S=1}^{8} \sum_{\theta_0=1}^{8} \sum_{k=1}^{24} [\Delta F_{loss}(\zeta_0, \theta_S, \theta_0, \rho_k)], \tag{22}$$

$$M_{orb} = \sum_{\zeta_0=1}^{22} \sum_{\theta_S=1}^{8} \sum_{\theta_0=1}^{8} \sum_{k=1}^{24} [\Delta M_{loss}(\zeta_0, \theta_S, \theta_0, \rho_k)], \tag{23}$$

$$E_{orb} = \sum_{\zeta_0=1}^{22} \sum_{\theta_S=1}^{8} \sum_{\theta_0=1}^{8} \sum_{k=1}^{24} [\Delta E_{loss}(\zeta_0, \theta_S, \theta_0, \rho_k)]. \tag{24}$$

Any summation of the momentum loss fractions over the directional cosine $\zeta_0$ will obviously have to be treated as positive or negative. We use the convention of $\zeta_0 > 0$ as being a positive momentum loss fraction. Additionally, we may construct cumulative distributions by integrating the summed distributions over successive flux surfaces

$$F_{cml}(\rho_0) = \int_{z=1}^{24} \sum_{\zeta_0=1}^{22} \sum_{\theta_S=1}^{8} \sum_{\theta_0=1}^{8} \sum_{k=z}^{24} [\Delta F_{loss}(\zeta_0, \theta_S, \theta_0, \rho_k)]. \tag{25}$$

We will make use of these summation methods to investigate the distribution of ions, energy, and momentum in the next two chapters.

## CHAPTER 5

# DISTRIBUTION OF ION-ORBIT-LOSS IONS AND ENERGY OVER THE SCRAPE-OFF LAYER

Using the full ion and energy differential loss fractions $\Delta F_{loss}(\zeta_0, \theta_S, \theta_0, \rho_k)$ and $\Delta E_{loss}(\zeta_0, \theta_S, \theta_0, \rho_k)$, as determined in the previous chapter, we can generate their distributions over various dimensions (IOL momentum results will be presented in the next chapter). The ion and energy distributions are shown at each poloidal launch location ($\theta_0$) compared against calculations using a simpler allocation [10,13] in Figure 18. In the original method [10,13], for which the poloidal distribution of the lost ions was not a concern, the smallest minimum energy for loss through any exit location was assigned to a given launch $\theta_0$ on a given flux surface $\rho_k$, and the lowest of these minimum energies over the different launch $\theta_0$'s was taken as the minimum loss energy for the flux surface at $\rho_k$.

A generalized contour plot for ion and energy over poloidal launch locations ($\theta_0$) and directional cosines ($\zeta_0$) is provided in Figure 19. The difference in poloidal particle motion for ion and energy fluxes traveling along the helical magnetic field, as seen in Figure 15, is the source of the poloidal asymmetry seen in Figures 18 and 19 as well as the secondary peak at the outer midplane in Figure 18. The rapid poloidal ion motion on each flux surface (negative or positive depending on the directional cosine $\zeta_0$) shifted the loss out from the inner midplane ($\theta_0 = \pi$), the allocation over the poloidal launch locations used in the new method was designed to take this motion into account.

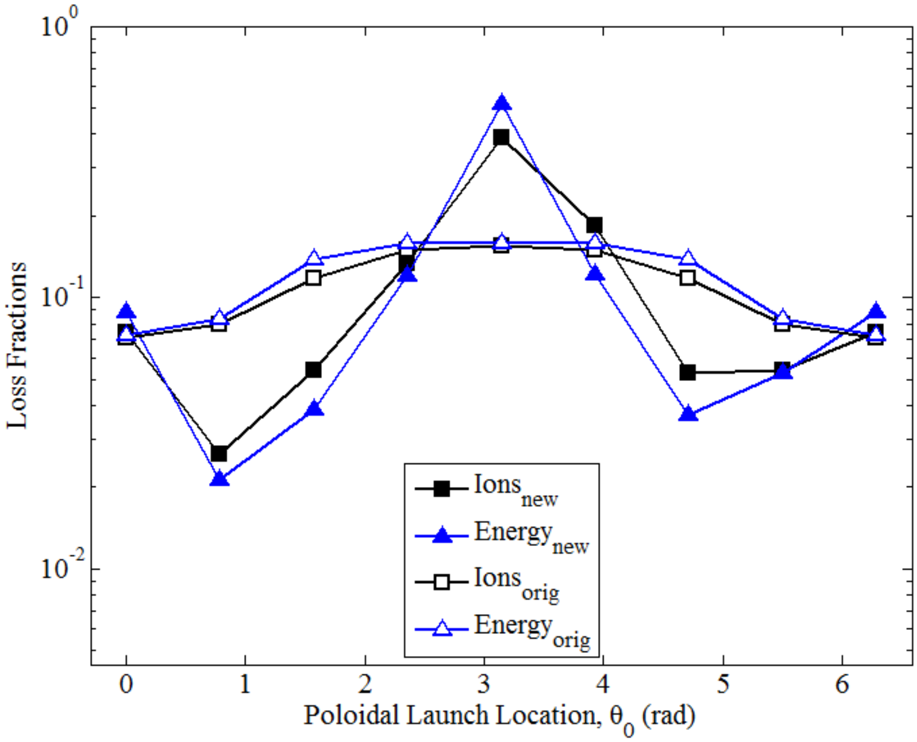

Figure 18. Ion and energy loss fractions at each poloidal launch location ($\theta_0$), compared with the original method [10,13].

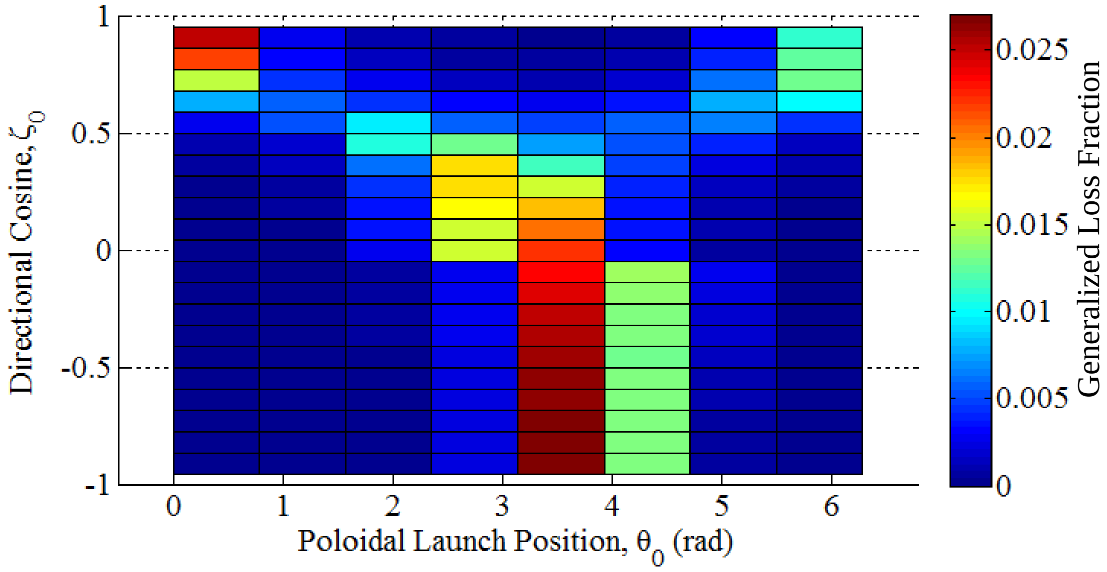

Figure 19. Contour plot for generalized ion and energy loss fractions at each directional cosine ($\zeta_0$) and poloidal launch location ($\theta_0$).

The ion and energy loss fractions for different poloidal exit locations ($\theta_S$) are shown in Figure 20. The peaking of the loss fluxes to the outboard midplane going into the SOL at $\theta_S$ = 0 is consistent with a previous estimate [13] and with experimental data [22-24]. This peaking at the outer midplane ($\theta_S$ = 0) on the separatrix for the new model is based upon the difference in minimum required energy at the outer midplane compared to the other poloidal exit locations ($\theta_S$), see Figures 5-10.

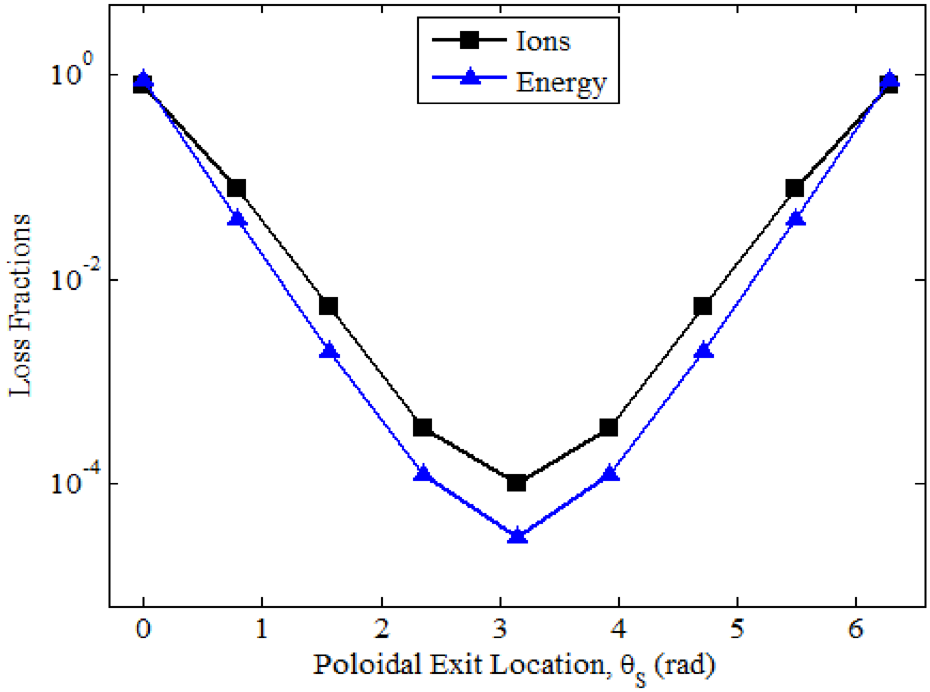

Figure 20. Loss fractions across separatrix for ions and energy at each poloidal exit location ($\theta_S$).

By taking the ratio of the local to the average energy at each poloidal exit location ($\theta_S$) from Figure 20 given by $\Delta E_{loss}(\theta_S)/\left(\left[\sum_{\theta_S=1}^{8}\Delta E_{loss}(\theta_S)\right]/8\right)$ we compare against the normalized radial conductive heat flux $q_r(r,\theta_S)/\langle q_r(r)\rangle$ going into the SOL [25] calculated with miller model geometry, see Figure 21. The poloidal distribution of particle or energy fluxes across the separatrix due to IOL is quite different than the distribution from conductive or diffusive transport in the plasma, as seen in Figure 21. Given that Figure 20 indicates that more than 95% of the energy flowing across the separatrix is due to IOL, this would seem to explain experimental observations of more energy going to the outer than inner divertor leg.

It should be noted that we have not included the X-loss of ions by grad-B and curvature drifting radially outward in the weak poloidal magnetic field region in the vicinity of the X-point [8], which would be expected to cause a secondary peaking in the IOL distribution in Figure 20 in the vicinity of the X-point at $\theta_S = \pm 3\pi/4$.

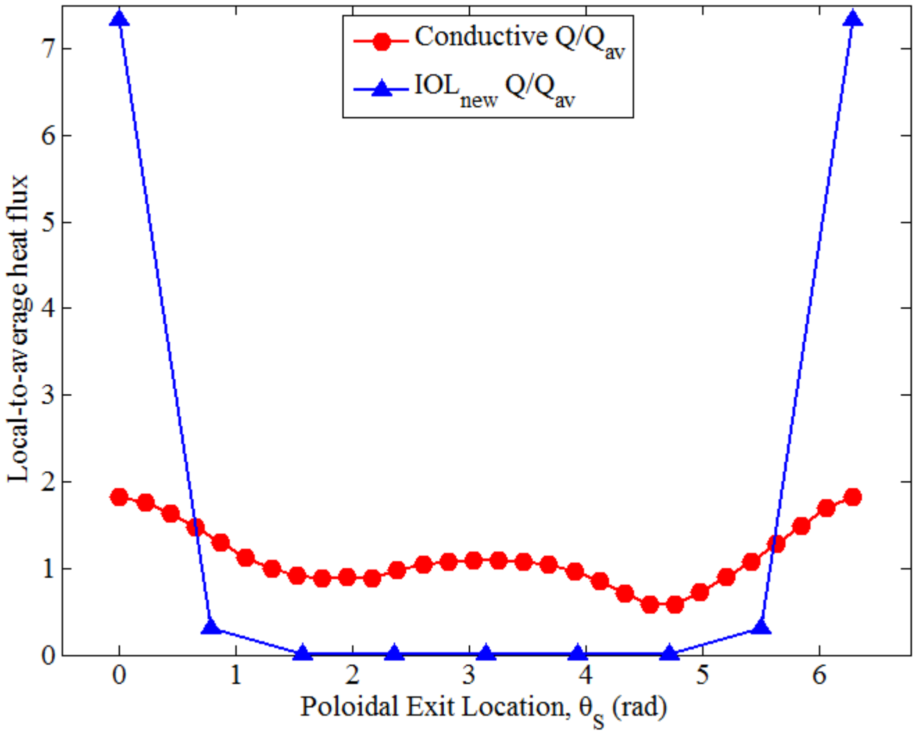

Figure 21. Predicted poloidal exit location ($\theta_S$) distribution of the conductive and IOL energy flux just inside the separatrix going into the SOL.

Cumulative ion and energy loss fractions at each radial flux surface position ($\rho_0$) are compared with the original methodology [10,13] in Figure 22. The new method allows more ions to be lost at each flux surface as ions at each poloidal launch position have access to other locations with lower minimum energy requirements. The higher loss rates seen in the last few flux surfaces for the new model are attributed to this.

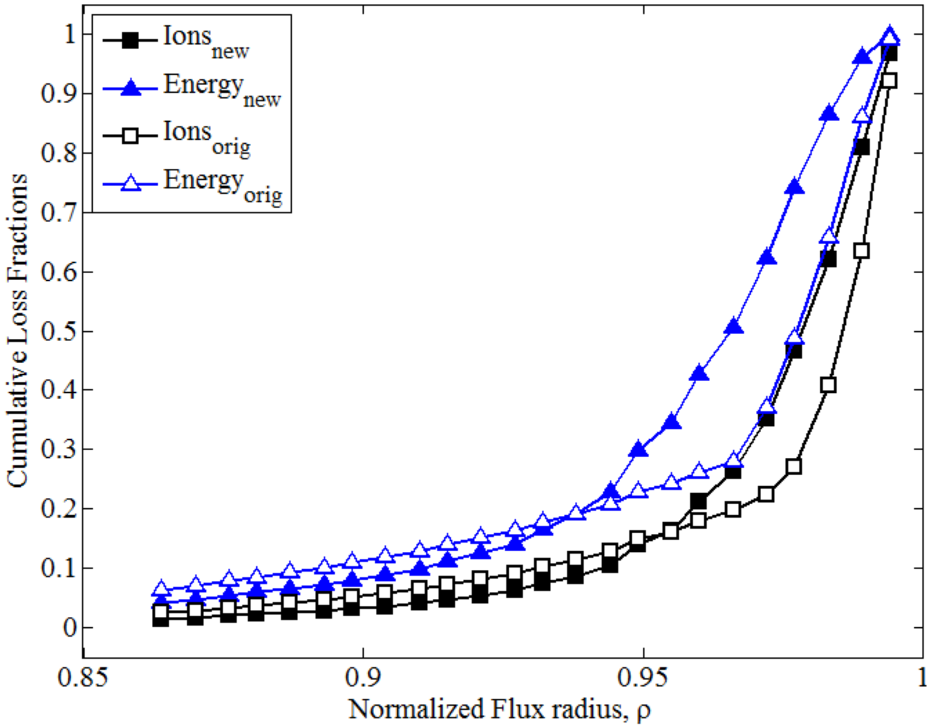

Figure 22. Cumulative loss fractions for ions and energy at each radial flux surface position ($\rho_0$).

We find the total cumulative loss fractions at the separatrix for the whole plasma to be $F_{orb}$ = 0.9683 and $E_{orb}$ = 0.9982. Thus, it seems that IOL plays a major role in creating the sources of particles, momentum and energy into the SOL, in this shot. If only half of the ions which undergo IOL to the separatrix are actually lost to (do not re-enter) the plasma then IOL still contributes the majority of these fluxes, much more so than from conduction or convection transport within the plasma.

## Estimating the Effect of Scattering

Scattering has been neglected to this point in the development of the ion-orbit-loss computational methodology. The 90-degree ion-ion scattering time in a typical DIII-D edge plasma is on the order of $\tau_{90}^{ii} \cong 10^{-4}s$, which is comparable to typical radial transport times, so scattering may have an effect.

Inclusion of scattering in the conservation equations would be impractical. However, we can estimate the effect of scattering by assuming that scattering isotropizes the velocity distribution.

Allowing ions to move from directional cosines with high minimum energy into other directional cosines ultimately moves the lowest energy ions (which can be lost on a given flux surface) to the directional cosine with the lowest overall minimum energy, $\zeta_0{}' \rightarrow \zeta \rightarrow \zeta_{0,Emin}$, where ions can be lost. We apply this scattering estimation method to the calculation of the differential loss fractions determined in the previous chapter. The following distributions will correspond to Figures 18, 20 and 22 in the previous section.

The ion and energy loss fractions at each poloidal launch location ($\theta_0$) are compared against the non-scattering data (without estimated scattering) in Figure 23. We omitted the contour plot at each poloidal launch location $\theta_0$ and directional cosine $\zeta_0$ for the estimated scattering data because it had only one peak at the outboard midplane in the extreme counter-current position. The ion and energy loss fractions at each poloidal exit location $\theta_S$ are compared against non-scattering data in Figure 24.

The predominant loss of ions from, and to, the outer midplane at $\theta_0 = 0$ and $\theta_S = 0$ with the scattering method (Figures 23 and 24) is due to ions scattering into the lowest minimum energy requirement region of the counter-current directional bins at the outer midplane, see Figures 5-9. Due to this scattering fewer non-lost ions remain which can meet the physical requirements to be lost from the co-current directional cosines which have higher energetic requirements. The severe lack of co-current ion loss, which occurs predominately at the inner midplane, is also the reason the magnitude of the poloidal asymmetry is different for the scattering method. The outer midplane peaking peaking for the new and scattering methods is consistent with the predictions of the original method [10,13] and with experimental data [22-24].

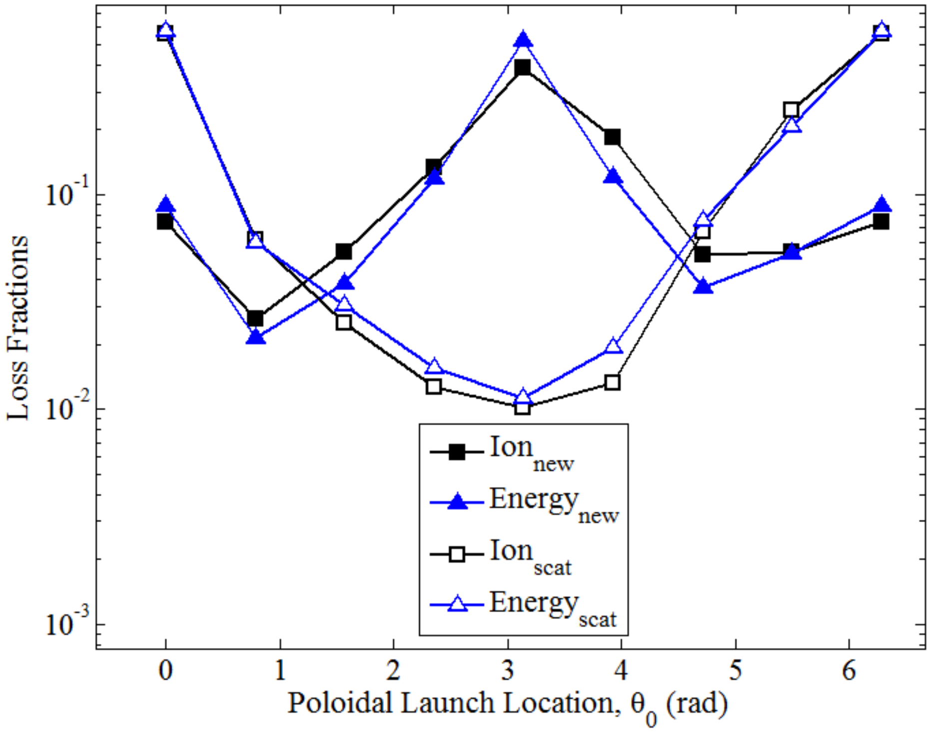

Figure 23. Ion and energy loss fractions for each poloidal launch point ($\theta_0$) with and without scattering.

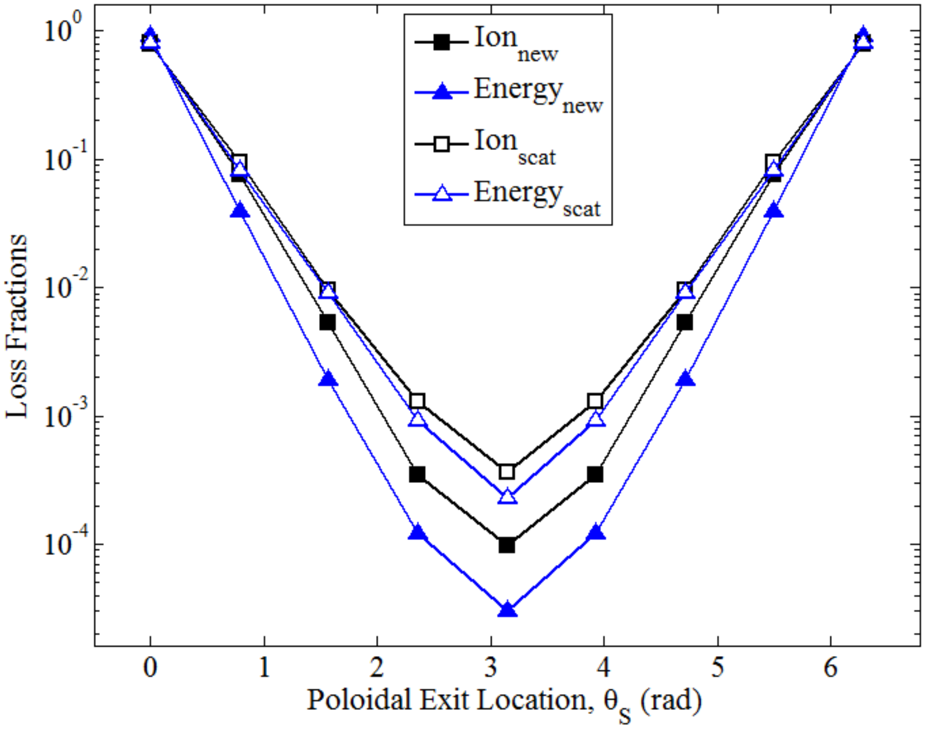

Figure 24. Ion and energy loss fractions at each poloidal exit location ($\theta_S$) with and without scattering.

The ion and energy loss fractions at each radial flux surface position are compared against non-scattering data in Figure 25. The change in curvature for the scattering method is due to additional ions being lost on each flux surface as ions were able to access directional cosines with lower minimum energy requirements.

The total overall loss fractions with estimated scattering for ion and energy are $F_{orb}$ = 0.9955 and $E_{orb}$ = 0.9999. These total loss fractions are higher than the non-scattering case due to more ions being lost from counter-current directional cosines with lower overall minimum energy requirements. It is clear that scattering increases the large fractions of ions and energy which are ion-orbit-lost, and Figure 25 provides an upper limit.

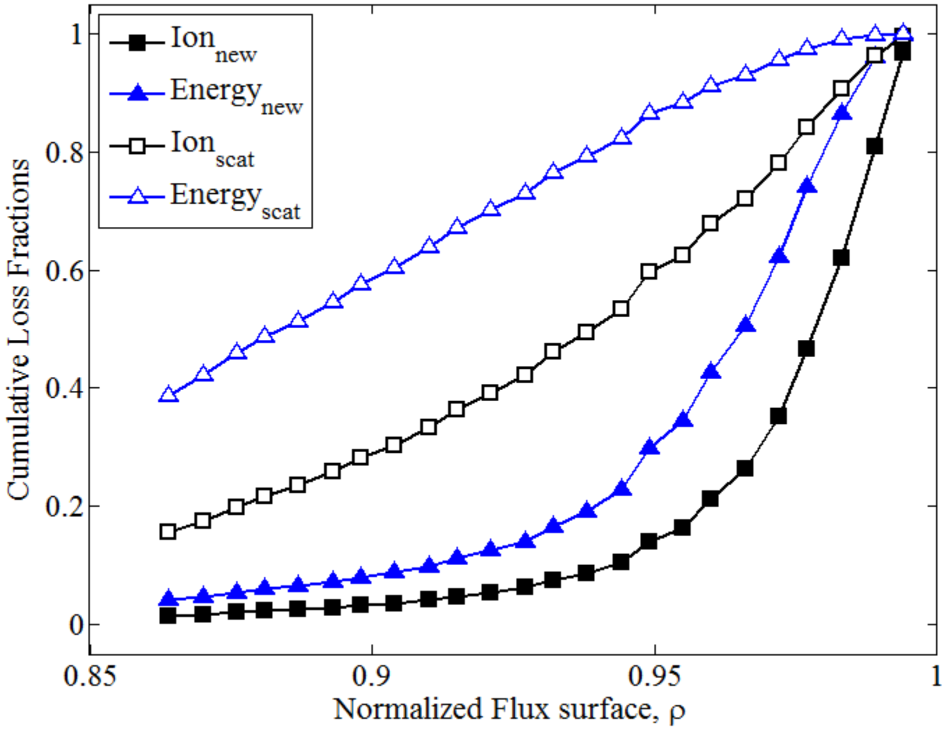

Figure 25. Cumulative ion and energy loss fractions at each radial position ($\rho_0$) with and without scattering.

# CHAPTER 6

# DISTRIBUTION OF MOMENTUM INTO THE SCRAPE-OFF LAYER AND INTRINSIC ROTATION

Using the allocated full differential momentum loss fraction $\Delta M_{loss}(\zeta_0, \theta_S, \theta_0, \rho_k)$ we can sum over selected dimensions to calculate momentum loss fraction distributions. The momentum loss fraction sign convention is based upon counter-current, $\zeta_0 > 0$, momentum loss resulting in a co-current spin up in the plasma edge. We define any summation of the differential momentum loss fraction over the directional cosine dimension as a net momentum loss fraction.

The cumulative distribution of net momentum loss fractions at each radial flux surface position ($\rho_0$) with the estimated scattering and original methods are shown in Figure 26. The final net momentum loss for the new model (last red filled in circle on Figure 26) is $M_{orb}$ = 0.0027, while the final net momentum loss with the scattering model (last hollow red circle in Figure 26) is $M_{orb,scattering}$ = 0.9245 (the original method was calculated to $M_{orb,original}$ = 0.0989). The intrinsic velocity, calculated from the net momentum loss fraction distribution, offers the best direct comparison with experimental data [15, 16, 17 and 18].

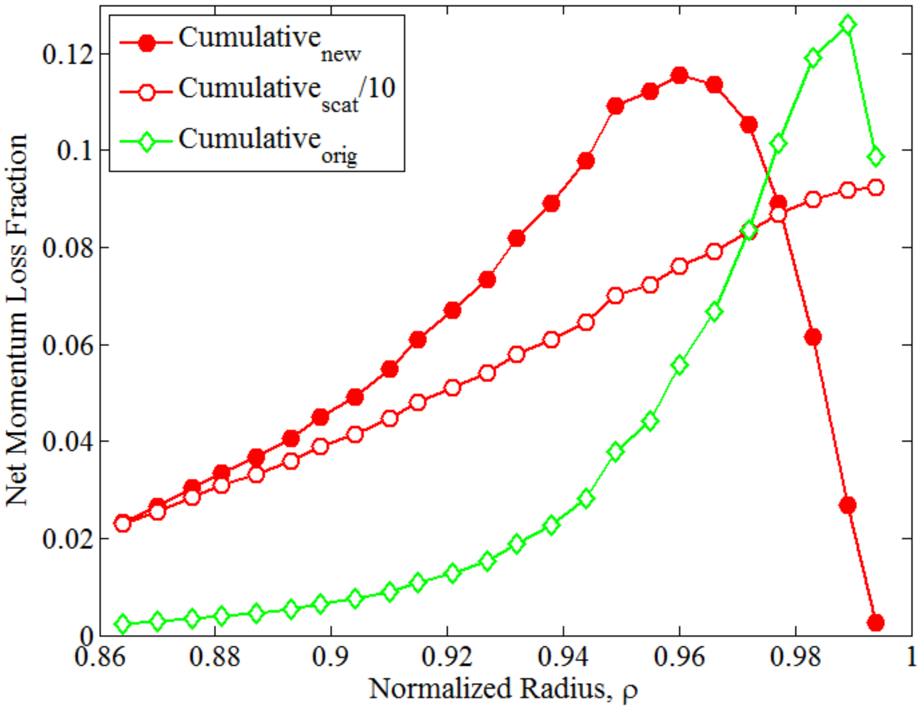

Figure 26. Cumulative net momentum loss fractions at each radial position ($\rho_0$) with scattering and original methods.

The intrinsic velocity may be solved for using the following equation from [12]

$$\Delta V_{||} = \frac{2\Gamma(2)}{\sqrt{\pi}} * M_{orb} * V_{th} = \frac{2}{\sqrt{\pi}} * M_{orb} * \sqrt{\frac{2kT_{ion}}{m}}, \tag{26}$$

where $M_{orb}$ or $\Delta M_{loss}(\zeta_0, \theta_S, \theta_0, \rho_0)$ are from Equation (23). Using Equation (26) we generate a plot similar to Figure 26 for the intrinsic plasma velocity, see Figure 27. The final intrinsic velocity (last red filled in circle on Figure 27) is 0.6 km/s, while the final intrinsic velocity with estimated scattering (last hollow red circle in Figure 27) is 200 km/s (the original method velocity came to 20 km/s).

A peaking of the toroidal rotation velocity inside the separatrix has been observed in a number of DIII-D shots [17-19] (to avoid further confusion we noted that the authors of Reference 19 used a different definition for the direction cosine which is opposite the convention used in the DIII-D papers they referenced).

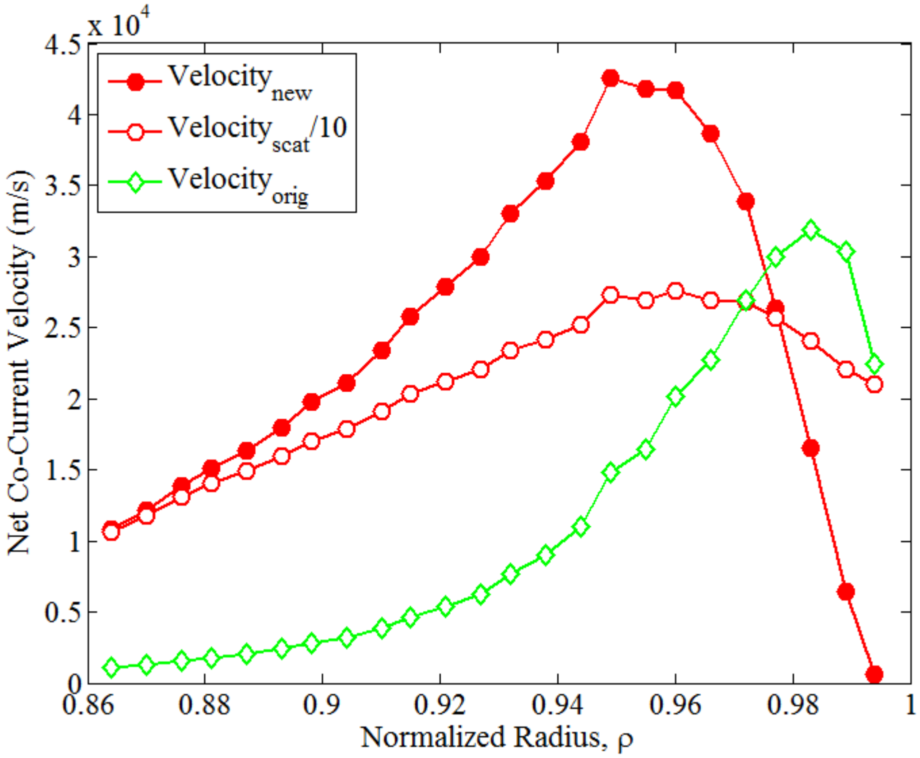

Figure 27. Net co-current velocity distributed over radial position ($\rho_0$) with scattering and original data.

The new model predicts broader peaking further away from the plasma edge (peaking at about $\rho_0 \cong 0.95$) than the original model (peaking at about $\rho_0 \cong 0.99$) while the experimental results estimate peaking in the vicinity of $\rho_0 \cong 0.98$ [17-19]. The peaking in both cases is due to the change in the major ion loss direction cosine starting with mostly counter-current directional cosine ion loss and then switching to mainly co-current directional cosine ion loss. For the new model more ions are lost at each flux surface so the major directional contributor to this loss (e.g. the counter-current direction cosine ions) are lost much faster than in the original model. The new model shifts from mainly loosing counter-current ions to co-current ions at an earlier flux surface than in the original as fewer non-lost counter-current ions are available in the last few flux surfaces. The broadness of the peaking in the new model is a side effect of having this shift sooner. The energy range of the ions in the new model when it shifts from mainly counter-current loss to co-current loss occurs just outside the energy range where the Maxwellian distribution peaks. This causes the peak to broaden as fewer co-current ions are available in the Maxwellian distribution at that energy range in comparison to where the original model peaks.

Since the original model demonstrated peaking closer to what the experimental results have predicted (peaking at about $\rho_0 \cong 0.98$ [17-19]) it is worth considering what assumptions in the new model may have shifted the peak further from the edge. Assuming our physical reasoning for the new model's behavior is correct then dampening the ion loss would shift the peak in the new model further out. To do this we consider the added major contributor to the ion loss in the new model, the second allocation method over poloidal launch locations. We previously assumed that ions at a given launch location ($\theta_0$) could travel poloidally (depending on their direction cosine $\zeta_0$) to other launch locations to be lost without restriction on the number of travels. However, if we restrict the number of times non-lost ions are allowed to travel poloidally we can lower the number of ions lost and shift the peaking out radially, see empty blue squares curve in Figure 28. We found restricting the poloidal travel distance to one rotation during the allocation over poloidal launch locations moved the new model into the closest agreement with the experimental results. It may be possible to add a feature into the new model later allowing greater resolution on this peak shifting.

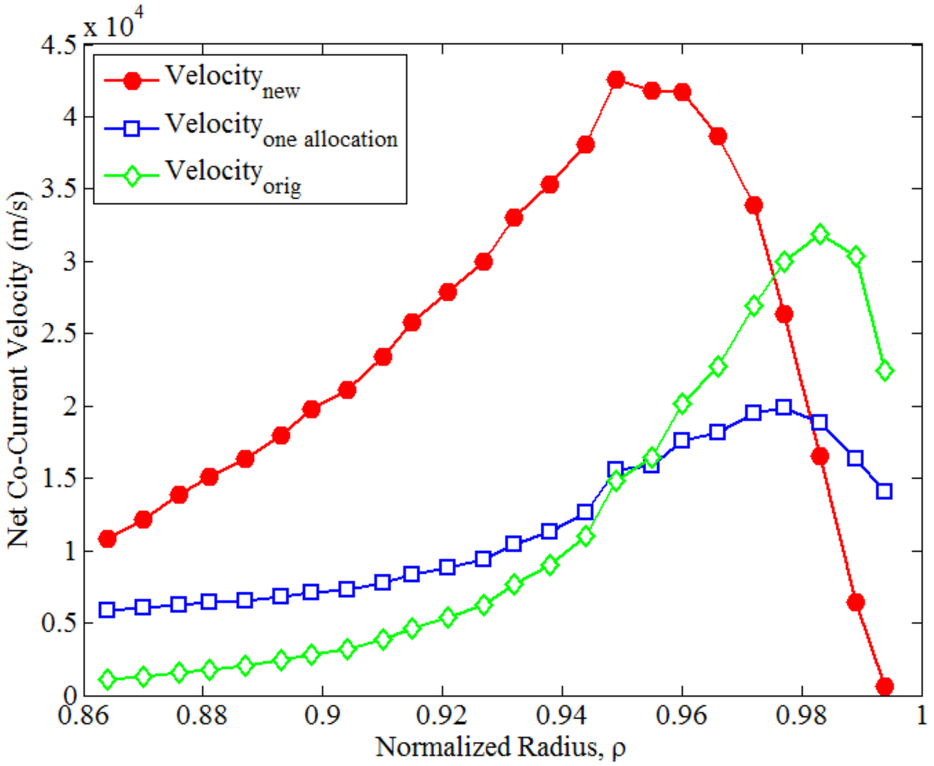

Figure 28. Net co-current velocity at each radial position ($\rho_0$) with a proposed one allocation step method and the original method.

The scattering model does not demonstrate any peaking whatsoever for the net momentum, see Figure 26, and far broader peaking at an order of magnitude higher in intrinsic velocity, see Figure 27. This is likely due to the majority of ions being lost within the lowest energy $E_{\min lowest}(\rho_0, \zeta_0)$ direction cosine ($\zeta_0$ = 0.955). There is an extreme peaking of the scattering model net momentum when viewed at each poloidal exit location ($\theta_S$) in comparison to the new model, see Figure 29. Most of the loss for both models goes to the vicinity of the outboard midplane ($\theta_S$ = 0 and ±π/4). The new model begins to lose co-current ions at the lowest energy location first ($\theta_S$ = 0) while the scattering model continues to lose ions in the counter current direction (which has the lowest energy requirement at $\theta_S$ = 0) thus creating the large peak. Additionally, the scattering model isotropization washes out the co-current and counter-current distinction that causes the peaking in the other models. This evidence argues against including the scattering as a major contributor for our calculation of IOL.

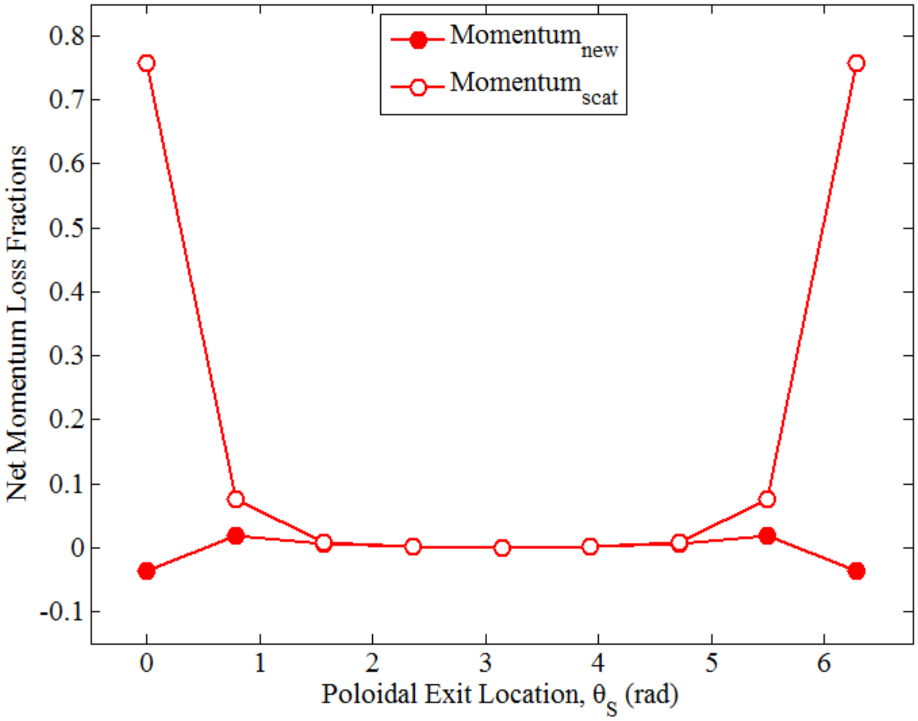

Figure 29. Net momentum loss fractions at each poloidal exit location ($\theta_S$) with the scattering method.

# CHAPTER 7

# SUMMARY AND CONCLUSIONS

In this thesis we introduced a new method for determining ion, momentum and energy fully differential loss fractions by new allocation schemes over the poloidal exit and launch locations. The ions at each internal flux surface location with energy below the minimum required energy to execute and orbit out to a position on the separatrix are lost on these orbits or rotated poloidally to another location where they could be lost from the main plasma. This new allocation method enabled us to develop a more accurate method of representing the loss of particles, energy and momentum by internal ions which access orbits that leave the plasma.

The total ion-orbit-loss of ion and energy fluxes into the SOL generally matched the original model [10,13], though new asymmetries were found across the poloidal launch positions. The poloidal distribution of the energy flux into the SOL was very different for IOL than the conductive/diffusive energy flux distribution [25]. Additionally, IOL contributed the majority of the loss into the SOL far higher than any other single loss mechanism (e.g. conduction or convection). This has substantial implications for modeling and interpreting divertor physics in tokamaks (e.g. higher energy load to outboard divertor leg).

We found that estimating scattering did not significantly aid the new model in predicting co-current velocity experimental results, and we are generally inclined to neglect it, but the issue is not resolved. Our new model showed general agreement with the original in predicting intrinsic velocity peaking, though the new model predicted peaking deeper in the plasma edge and more broadly. We also confirmed previous predictions of [15] that IOL in an H-mode plasma with oppositely directed toroidal field and current produces an intrinsic co-current rotation in the edge plasma.

The results presented in this thesis are noted to be for an H-mode discharge in the DIII-D tokamak and would be expected to vary for other plasma and machine physical and geometric characteristics.

# APPENDIX A

# DERIVATION FOR THE SOLID ANGLE BINNING USED IN THIS RESEARCH

The directional cosine $\zeta_0$ values used in this research were chosen to be at the center of a evenly distributed set of 22 directional bins from -1 to 1, see Figure 30.

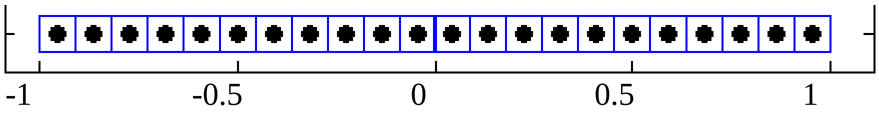

Figure 30. The 22 directional cosine bins used for this research.

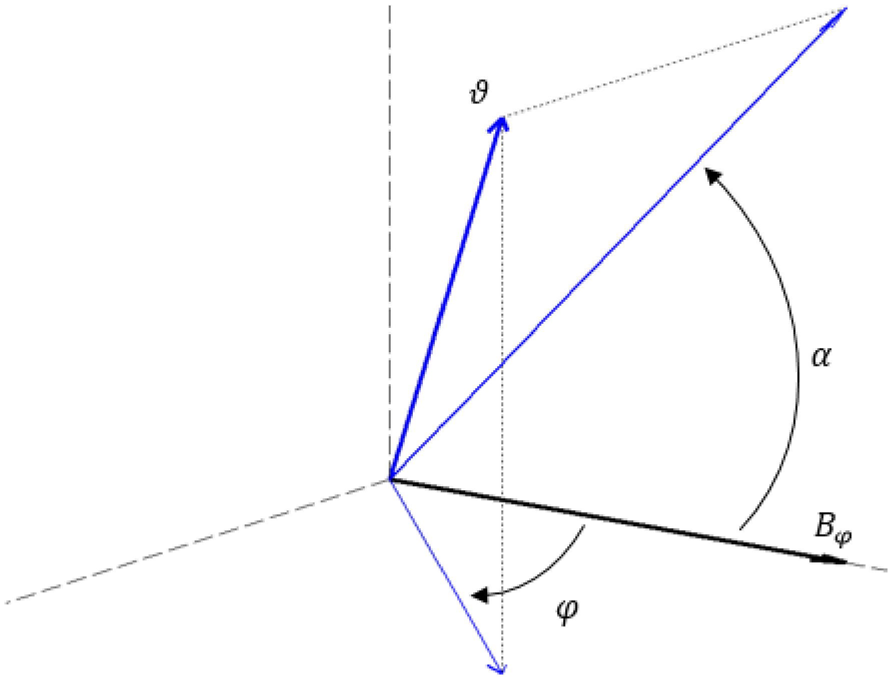

Figure 31. Azimuthal $\alpha$ and polar $\varphi$ angles of velocity $\vartheta$ relative to the toroidal magnetic field $B_\varphi$.

As a justification for this consider the equation for the solid angle over a sphere,

$$\Omega = \iint_S \sin\alpha \, d\alpha d\varphi. \tag{27}$$

The azimuthal angle $\alpha$ and polar angle $\varphi$ are shown in Figure 31 relative to the toroidal magnetic field, $B_\varphi$, and a sample velocity, $\vartheta$. For our calculation, the polar angle ($\varphi$) can be arbitray for a given ion, so we can generalize the solid angle formula for each directional bin to that of a spherical cap or cone with a given azimuthal angle (α). This results in the solid angle equation for a cone with its vertex at the center of a sphere.

$$\Omega = 2\pi(1 - \cos(\alpha)) \tag{28}$$

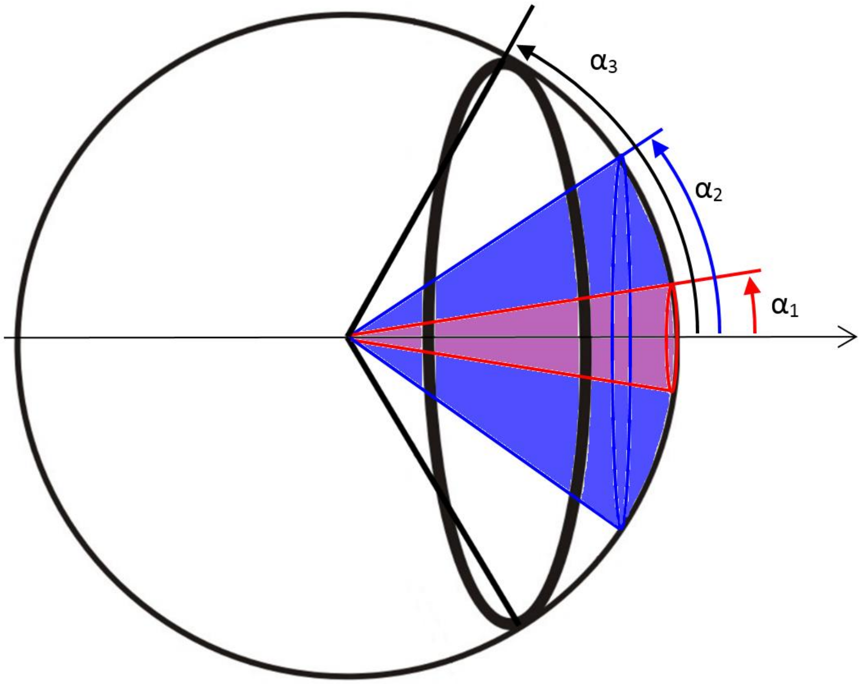

Figure 32. Nested cones with their enclosed solid angles projected onto a sphere.

The solid angle between two nested cones with their vertices at the center of a sphere, see Figure 32, is given by,

$$\Omega = 2\pi[(1-\cos(\alpha_n)) - (1-\cos(\alpha_{n-1}))]. \tag{29}$$

In order to generate the 22 evenly sized differential areas of the solid angle we make use of Equation (29), which we can further simplify by substituting $\zeta = \cos(\alpha)$ in for the directional cosine.

$$2\pi \sum_{n=1}^{22}[(1-\cos(\alpha_n)) - (1-\cos(\alpha_{n-1}))] = 4\pi \tag{30}$$

$$\sum_{n=1}^{22}[(1-\zeta_n) - (1-\zeta_{n-1})] = \frac{4\pi}{2\pi} \tag{31}$$

Since we want each of the 22 solid angle bins to be the same size we set up the following relationship for the size of any given solid angle bin.

$$[(1-\zeta_n) - (1-\zeta_{n-1})] = constant = \frac{1}{11}, \text{ where } 1 \leq n \leq 22 \tag{32}$$

Using Equation (32) we can solve for the left edges of the 22 solid angle bins in terms of the directional cosine, $\zeta$. For example consider the following application of Equation (32) to the calculation of the left edges for the first two directional bins.

$$[(1-\zeta_1) - (0)] = \frac{1}{11}$$

$$(1-\zeta_1) = \frac{1}{11} \rightarrow \zeta_1 = \left(1-\frac{1}{11}\right) = \frac{10}{11} = \text{Left edge for bin 1.}$$

$$[(1-\zeta_2) - (1-\zeta_1)] = \frac{1}{11}$$

$$\left[(1-\zeta_2) - \frac{1}{11}\right] = \frac{1}{11}$$

$$(1-\zeta_2) = \frac{2}{11} \rightarrow \zeta_2 = \left(1-\frac{2}{11}\right) = \frac{9}{11} = \text{Left edge for bin 2.}$$

We pick a center point for each bin to use as a representative point for each bin such that half of each bin's solid angle can be found to either side of the center point.

$$(1-\zeta_{center}) - \left(1-\zeta_{right\ edge}\right) = constant$$

$$constant = \left(1-\zeta_{left\ edge}\right) - (1-\zeta_{center}) = \frac{1}{22} \tag{33}$$

Using Equation (33) in conjunction with Equation (32) we can now calculate the center point values for each solid angle bin in terms of the directional cosine. Using the left bin edges we calculated in the previous example we calculate the center points for the first two bins.

$$\left(1-\frac{10}{11}\right)-(1-\zeta_{center})=\frac{1}{22}$$

$$\zeta_{center}-1=\frac{1}{22}-1+\frac{10}{11}$$

$$\zeta_{center}=\frac{1}{22}+\frac{10}{11}=\frac{21}{22}=\text{Center for bin 1.}$$

$$\left(1-\frac{9}{11}\right)-(1-\zeta_{center})=\frac{1}{22}$$

$$\zeta_{center}-1=\frac{1}{22}-1+\frac{9}{11}$$

$$\zeta_{center}=\frac{1}{22}+\frac{9}{11}=\frac{19}{22}=\text{Center for bin 2.}$$

By choosing equal sized solid angle bins we ensure that an equal number of ions are contained inside each directional bin and thus represented by each of the directional cosines that we sample over, since we assume that at least initially the ions are isotropic. Applying this directional binning to the energy distribution curve we effectively split it into 22 curves, which are all roughly a fraction 1/22 or 4.455% of the full curve, see Figure 33. Summing over a single one of these curves from zero to infinity will yield 1/22 and summing over all of them from 0 to infinity will yield 1 like the full Maxwellian.

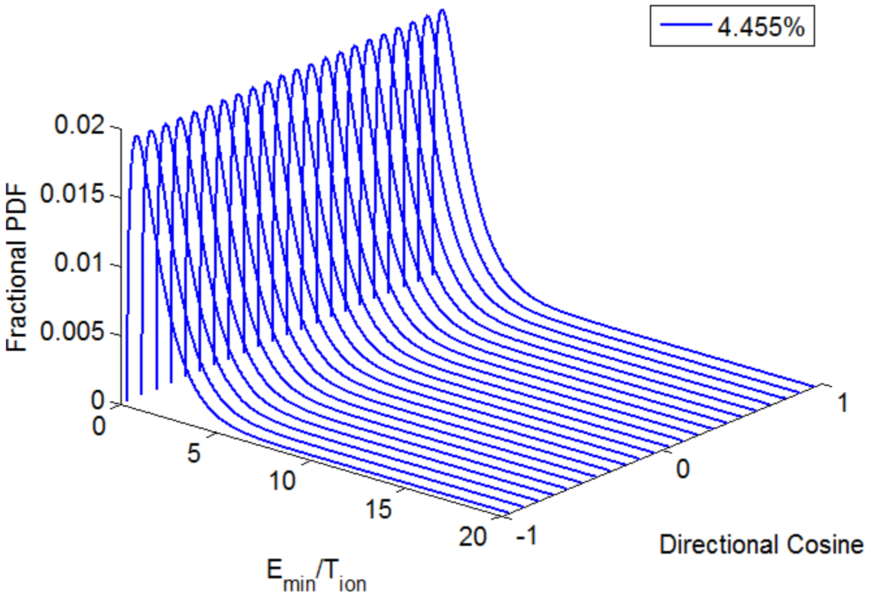

Figure 33. Maxwellian PDF for a uniformly sampled loss cone.

If we ever wanted to use a non-uniform distribution of directional cosine sampling, something similar to Figure 30 but with blue boxes of different sizes, then we could use the following factor, $f(\zeta_i)$, in place of the 1/22 that was mentioned previously.

$$f(\zeta_i) = \frac{abs\left(abs\left(\frac{\zeta_{i-1}+\zeta_i}{2}\right)-abs\left(\frac{\zeta_i+\zeta_{i+1}}{2}\right)\right)}{2} \tag{34}$$

# REFERENCES

[1] Hinton F.L. and Chu M. *Nucl. Fusion* 25, 345 (1985).

[2] Shaing K.C. and Crume E.C. 1989 *Phys. Rev. Lett.*63, 2369 (1989).

[3] Shaing K.C., Crume E.C. and Houlberg W.A. *Phys. Fluids* B 2, 1492 (1990).

[4] Shaing K.C. *Phys. Fluid* B 4, 171 (1992).

[5] Shaing K.C. *Phys. Plasmas* 9, 1 (2002).

[6] Miyamoto K. *Nucl. Fusion* 36 ,927 (1996).

[7] Matthews G.F., Corrigan G., Erents S.K., Fundamenski W.,Kallenbach A., Kurki-Suonio T., Sipila S. and Spence J. *JET Report* EFDA-JET-CP(02)01-02 (2002).

[8] Chang C.S. *et al* *Phys. Plasmas* 9, 3884 (2002).

[9] McClemente K.G. and Thyagaraja A. *Phys. Plasmas* 13, 042503 (2006).

[10] Stacey W.M., *Phys. Plasmas* 18. 102504 (2011).

[11] Stacey, W. M., Groebner, R. J. and Evans, T. E., *Nucl. Fusion* 52, 114020 (2012).

[12] Stacey, W. M., Sayer, M-H., Floyd, J-P. and Groebner, R. J., *Phys. Plasmas* 20, 012509 (2013).

[13] Stacey W.M. *Nucl. Fusion* 53, 063011 (2013).

[14] Floyd, J-P., Stacey, W. M, Groebner, R. J. and Mellard, S. C., “Evolution of edge pedestal ransport between ELMs in DIII-D”, *Phys. Plasmas* (submitted) 2014.

[15] deGrassie J.S., Groebner R.J., Burrell K.H. and Solomon W.M. *Nucl. Fusion* 49, 085020 (2009).

[16] deGrassie J.S., Muller S.H. and Bodeo J.A., *Nucl. Fusion* 52, 013010 (2012).

[17] Stacey, W. M.,Boedo, J. A., Evans, T. E., Grierson, B. A., and Groebner, R. J., *Phys. Plasmas* 19, 112503 (2012)

[18] Stacey, W. M. and Grierson, B. A. , *Nucl. Fusion* 54, 073021 (2014).

[19] Pan, C., Wang, S. and Ou, J., *Nucl. Fusion* 54, 103003 (2014).

[20] Stacey, W. M. and Pan, C., “Correction of NF54, 103003 (2014)”, *Nucl. Fusion* (2015).

[21] Luxon J., *Nucl. Fusion* 42, 614 (2002).

[22] Petrie T.W. et al., *Nucl. Mater*. 313–316, 834 (2002).

[23] Petrie T.W. et al., *Nucl. Mater*. 337–339, 216 (2005).

[24] Petrie T.W., Watkins J.G., Lao L.L. and Snyder P.B., *Nucl. Fusion* 43, 910 (2003).

[25] Stacey, W. M. and Bae C., *Phys. Plasmas* 16, 082501 (2009).